Republic of Iraq
Ministry of Higher Education and Scientific Research
University of Babylon
College of Engineering
Civil Engineering Department

Regional Weather Variation Effect on Land Use /Land Cover Using Geographic Information System

A Thesis
Submitted to the Department of Civil Engineering, College of Engineering, University of Babylon in Partial Fulfilment of the Requirements for the Master Degree in Engineering/Civil Engineering/Water Resources

By:

Mohammed Hussein Younus Hussein

Supervised by

Prof. Dr. Ruqayah Kadhim Mohammed

2023 A.D **1445 A.H**

بِسْمِ اللَّهِ الرَّحْمَنِ الرَّحِيمِ

هُوَ الَّذِي بَعَثَ فِي الْأُمِّيِّينَ رَسُولًا مِنْهُمْ يَتْلُو عَلَيْهِمْ آيَاتِهِ وَيُزَكِّيهِمْ وَيُعَلِّمُهُمُ الْكِتَابَ وَالْحِكْمَةَ وَإِنْ كَانُوا مِنْ قَبْلُ لَفِي ضَلَالٍ مُبِينٍ"

صدق اللَّهُ العلي العظيم

سورة الجمعة {الأية: ٢}

Supervisor Certification

I certify that this thesis, which is entitled (***Regional Weather Variation Effect on Land Use /Land Cover Using Geographic Information System***), has been prepared by ***Mohammed Hussein Younus*** under my supervision at the College of Engineering, Babylon University, in partial fulfilment of the requirements for the degree of Master of Science in Water Resources Engineering.

Signature:

Name: ***Prof. Dr. Ruqayah Kadhim Mohammed***

Date: / / 2023

EXAMINATION COMMITTEE CERTIFICATE

We certify that we have read this thesis entitled ***"Regional Weather Variation Effect on Land Use /Land Cover Using Geographic Information System "*** presented by **"Mohammed Hussein Younus Al-Khafaji"** and as an examining committee, we examined the student in its content and in what is connected with it, and that, in our opinion, it meets the standard of a thesis for the degree of Master of Science in Civil Engineering/Water Resources Engineering.

Signature:

Name: ***Prof. Dr. Ruqayah Kadhim Mohammed***

(Supervisor and Member)

Date: / /

Signature:

Name: **Asst. Prof. Dr. Imad H. Obead**

(Member)

Date: / /

Signature:

Name: **Asst. Prof. Dr. Riyadh H. Mohammed**

(Member)

Date: / /

Signature:

Name: **Prof. Dr. Shaymaa A. M. Hashim**

Date: / /

(Chairman)

Approval of Head of the Civil Engineering Department

Signature:

Name: ***Asst. Prof. Dr. Zaid H. Majeed Al-Hasoon***

Date: / /

Approval of Deanery of the college of Engineering

Signature:

Name: ***Prof. Dr. Laith Ali Abdul-Rahaim***

Date: / /

Deduction

“To the immaculate imams (may the best of greetings and peace be upon them), To my faithful wife, who supported and encouraged me in my time of giving up”

"To everyone who helped me move the rocks on my way there, to ever yone who believed in me"

With love and respect

Mohammed Hussein

Acknowledgements

In the name of Allah, the Most Gracious, the Most Merciful Praise be to Allah for the blessing he has bestowed upon me, and prayers and peace be upon the one who was sent with mercy, upon his family, and upon his honorable companions and after.

"He who does not thank people does not thank God." When I put the final touches on my humble effort, which would not have seen the light of day without the strenuous efforts and careful follow-up of the sincere Professor ***Dr. Ruqayah Kadhim Mohammed****, "My supervisor and my support thanks to her after God, I completed my message, which spared no effort in helping me, may God reward her with the best reward, and for all appreciation and respect. I also do not forget the efforts made by all my teachers since I took my first steps in elementary school until today, especially my teachers in my department, the head of the department and all the people who put in hidden effort there.*

As I stand here, I cannot express my thanks enough for my support in life, ***my dear mother, my dear father****, and* ***my dear wife****, who supported me in order to fulfil my dream so that I could reach what I have reached with their prayers and encouragement.*

Finally, many thanks to ***all my family members****, my* ***best friends****, and everyone who helped me and who contributed to showing this effort for existence.*

Mohammed Hussein Younus

Abstract

Drought is a disaster that profoundly impacts several factors, including the economy, agriculture, environment, and society. In order to successfully monitor droughts in semi-arid regions, assessments of the severity and impact of droughts are required. However, little is known about how variations in yearly patterns and configurations of land use and land cover (LULC) influence the consequences of drought. LULC classification and drought evolution was evaluated and mapped by combining geographic information system and remote sensing techniques. The Diyala River Basin (DRB), north of Iraq, has been considered a representative study area. Five major LULC types were mapped: water bodies, urban lands, bare lands, vegetation lands and palm, depending on the Landsat imageries of 2013, 2016, 2019, and 2022. The images were categorised using a classification algorithm and a maximum likelihood method. The study results showed that during the study period, the urban lands and bare lands have expanded from 1295.8 km2 (3.9%) to 1677.4 km2 (5.1%) and 5770.3 km2 (17.5%) to 8501.1 km2 (25.8%), whereas the vegetation lands have declined from 25,273.9 km2 (76.6%) to 22,421.8 km2 (68.0%). Using spectral indices from Landsat, the current research also evaluated droughts' magnitude and frequency in the DRB during the growing season for 2013 through 2022. Fifteen mosaics were created over ten years using forty images in Landsat 8 and 9 OLI/TIRS (167/36 and 168/37) that had been gathered from 2013 to 2022. The scenes are from two Landsat time series. The drought situation was assessed using the Normalized Difference Vegetation Index (NDVI), Vegetation Condition Index (VCI), Soil Adjusted Vegetation Index, Normalized Difference Water Index (NDWI), and Land Surface Temperature (LST). The research's findings revealed a increased in the DRB's occurrence and severity of drought over the past ten years, especially in 2021 and 2022. However, between 2021 and 2022, the total vegetation covered based on NDVI decreased by 20.67% and 36.33%, respectively. In 2021 and 2022, the vegetation lands significantly decreased from average (28.48% and 12.82%, respectively). The VCI results showed that in 2022, there was a prolonged extreme drought extent of

5727.1 km2 (47.8%). The NDVI and LST are more closely correlated drought indices and are appropriate for use in arid and semi-arid areas to monitor drought with limited data. Derbendekan and Hemrin lakes, equally, experienced declines of 15.1%, 7.12%, and 108.38%, 143.33% in 2021 and 2022, respectively. Between 2013 and 2022, the DRB experienced an increase in drought, a decline in water body surface area, and a decrease in precipitation averages. This study will advance knowledge of the connections between drought indices from remote sensing and meteorology.

List of Contents

List of Figures

List of Tables

List of Abbreviations

Abbreviation	Description
BL	Bare land
CA	Cellular Automata
CP	Change Portion
DEM	Digital Elevation Model
DLK	Derbendikan Lake
DRB	Diyala River Basin
FAO	Food and Agriculture Organization
FC	Fraction of illustrative Change
GIS	Geographic Information System
HLK	Hemrin Lake
KI	Kappa coefficient
LST	Land surface temperature
LULC	Land Use Land Cover
MIR	Middle Infrared Reflectance
ML	Maximum Likelihood Classifier
NASA	National Aeronautics and Space Administration
NDVI	Normalized Difference vegetation Index
NDWI	Normalized Difference Built-up Index
NIR	Near Infra-Red
OA	overall accuracy
PA	Producer Accuracy
PL	Palms
RS	Remote Sensing
SAVI	Soil adjusted vegetation index

Abbreviation	Description
UA	User Accuracy
UL	Urban Lands
USGS	United States Geological Survey
VCI	Vegetation Condition Index
VL	Vegetation land
WB	Water Bodies

CHAPTER ONE
INTRODUCTION

1.1 General

Climate change has primarily impacted land use and land cover (LULC), impacting worldwide temperatures and precipitation (Al-Timimi et al., 2012; Sameer et al., 2023). The LU and LC modifications are helpful for analysis and visualization of the impact of different advance routes and aid in the formulation of scientific policies (Degife et al., 2019) and the implementation of tenable laws that protect natural resources and offer ecosystem services (Hailu et al., 2018; Hussain and Karuppannan, 2021). The main concern is how directly LULC affect the Earth's fundamental processes and features, such as the water cycle, biological habitats, and land degradation and production (Goward et al., 2002). The current condition of the Earth's surface appears to be drastically changing due to anthropogenic activity (Hussain et al., 2022; Mohy an Rasheed, 2022; Sayl et al., 2022). By reducing ecological infrastructure, the LULC alterations heightened the interplay of resources, administrative concerns, and humanities in responding to climate change and socioeconomic calamities (Saleh and Ahmed, 2021).

Remote sensing data may be the only information source for drought monitoring in locations with few sampling gauges (Julien and Sobrino, 2010; Juliev et al., 2019; Sameer et al., 2021, 2023). Globally, drought intensity, duration, and impact have all been measured using satellite-based drought indices, such as the Normalized Difference Vegetation Index (NDVI), Vegetation Condition Index (VCI), and Land Surface Temperature (LST) (Goward et al., 2002; Gaznayee and Al-Quraishi, 2019; Hussain et al., 2020a; Dibaba et al., 2020; Gaznayee et al., 2021; Mohammed and Sayl, 2021).

The NDVI, which deals with the robustness of vegetation and has a strong link with green biomass, an indicator of healthy vegetation or crops, was calculated mathematically utilizing spectral bands inside the satellite picture (Saleh and Ahmed, 2021; Hussain et al., 2020b). The NDVI creates an adaptable way to calculate plants' amount, value, and growth by relating near-infrared and red colour spectral information (Yesuph and Dagnew, 2019). High-resolution satellites such as the Landsat series, the Sentinel series, and various on-board sensors are currently available to estimate the vegetation index at local (Mustafa 2020) and universal levels (Dibaba et al., 2020; Hussien and Karuppannan, 2022; Mohammed et al., 2022).

The Vegetation Condition Index (VCI) was created to separate ecological and weather-related signals in the NDVI. Gaznayee et al. (2021) results highlight relationships with some ecological variables and demonstrate the VCI's ability to detect characteristics of droughts, providing crucial data to decision-makers in the environmental and economic sectors. Furthermore, Land Surface Temperature (LST) measures the energy balance of the earth's surface, providing vital information about the physical properties and climate of the planet (Arsyad et al., 2018; Assaf et al., 2021).

Gaznayee et al. (2022) reported a negative correlation between LST and NDVI, as an increase in LST was observed at several scales due to changes in vegetation cover and soil moisture, indicating that surface temperatures can rise rapidly with water stress. According to Sun et al., 2010, and Mohammed and Sayl, 2020 Recent whose described the correlation between NDVI and LST, which is one of many factors that negatively affect vegetation dynamics, as an essential element.

1.2 Statement of Problem

The Diyala River Basin, which have an area of 32,600 km^2 and is 445 km long, is the third-largest tributary of the Tigris River. The river serves as Diyala City's main water source for domestic, agricultural, municipal, and other uses. Water contamination and scarcity are current issues in the Diyala River Basin. Several changes have recently been made to the river basin. It is crucial to identify and categorize the basin's LULC for planning and management in the area to preserve the best opportunity given the rise in land use brought on by a population boom and urbanization linked to climate variability.

Understanding the causes, processes, and generalizations of LULC alteration at many spatiotemporal levels is essential for researching these topics (Dibaba et al., 2020). Doing so would make it easier to compare different catchment areas and pinpoint those vulnerable to change. This would assist decision-makers in using more practical methods to maintain the water resources while drawing significant attention to the basin environment.

1.3 Aim and Objectives

The main aim of this study is to investigate the pattern and evolving characteristics of land use and land cover in the Diyala catchment, northern Iraq, from 2013 to 2022. Therefore, the specific study objectives are :

(1) Identify land use and land cover variations; and

(2) Determine the status and frequency of droughts by estimation the Normalized Difference Vegetation Index, Vegetation Condition Index, and Land Surface Temperature alterations. in the Diyala River basin over the last ten years (2013–2022) using remote sensing methods.

1 .4 Assumptions and Limitations

Studying the drought condition of the study area using the NDVI, VCI, NDWI, and NDBI indices, and using aerial images downloaded from the USGS (https://earthexplorer.usgs.gov), with a spatial resolution of 30 meters. Despite this resolution can be considered low accuracy, but for the present work purposes, it was suitable to trace the LULC alterations. Downloading and implement the amount of precipitation and temperature data from NASA (http://power.larc.nasa.gov) because of shortage of ground weather stations historical records. A period of every 3 years was also taken to detect changes in LULC, as well as to estimating NDBI and SAVI, and a period of each year was taken to determine the values of NDVI, NDWI, and VCI, which is considered a good period to measure the state of drought and the difference in vegetation cover, as well as the variation in water bodies in the DRB over the study period.

CHAPTER TWO

Theory and Review of Literature

2.1 Introduction

Climate change has mostly impacted land use and land cover around the world due to changing temperatures and precipitation levels (Al-Najjar et al., 2019, Pradhan et al., 2020). Which in turn changes in land use and land cover (LULC) have an effect on both physical and human ecosystems, and they also contribute to climate change. It is important in many socioeconomic and environmental applications. Additionally, it affects streamflow. Data on long-term LULC change are essential for managing water resources and urban development because of population growth and water scarcity. Numerous prior studies looked at how changes in land use and land cover impact hydrological processes and how to forecast future map. This chapter will provide an in-depth but concise review of relevant local and global previous studies on LULC alteration.

2.2 Remote Sensing

The science of remote sensing focuses on the investigation of interaction of electromagnetic waves with items on the ground, and the detection, analysis, and exposes the properties of distinct elements' spatiotemporal variations and land area, using technology for classification of remote sensing photos is a crucial way to identify and interpret target features is now one of the techniques for researching changes in land use successful (Peijun et al., 2016).

2.3 Land Use and Land Cover

The Earth's and its immediate surroundings' physical and biophysical characteristics are referred to as Land Cover (LC). It is represented by the distribution of the land's physical features, including those created only by human activity, like settlements, such as vegetation, water, desert, and ice. However, the

phrase Land use (LU) refers to how people intend to use or manage a specific type of LC. Therefore, LU includes both the method by which the biophysical characteristics of land are modified and the intention behind that modification (the purpose for which the land is used, such as agriculture, grazing, etc.). These more subtle changes affect the character of the LC without changing its overall classification. This definition of LU establishes a direct link between human behavior and the LC (FAO, 1998a).

A detailed investigation is required for effective LC management. Several academic fields, including biology and soil sciences, hydrology, and meteorology, have knowledge of the physical characteristics of the LC based on direct measurements and the use of physical models (Hagos, 2014). The LC changes as a result of human modifications to the earth's surface. These changes have a significant impact on how key components of the Earth's system function (such as energy, water, and soil balance). In addition, as the population grows, the demand for finite natural resources rises, changing the surface of the land (Islam et al., 2018). An important factor in the creation of runoff is the impact of LC, as the amount of water that is intercepted for infiltration and runoff depends on the vegetation that divides the water (Winnaar et al., 2007).

Climate change, which has altered global temperatures and precipitation levels, has had the greatest impact on LULC (Al-Timimi et al. 2012; Sameer et al. 2023). The LULC modifications are helpful for analysis and visualization of the impact of different advance routes and aid in the formulation of scientific policies (Degife et al. 2019). They also aid in the implementation of tenable laws that protect natural resources and offer ecosystem services (Hailu et al. 2018; Hussain and Karuppannan 2021). The main concern is how directly LULC affect the Earth's fundamental processes and features, such as the water cycle, biological habitats, and land degradation and production (Goward et al. 2002). The current condition of the Earth's surface appears to be drastically changing due to anthropogenic activity (Hussain et al., 2022; Mohy and Rasheed, 2022; Sayl et

al., 2022). By reducing ecological infrastructure, the LU, and LC alterations heightened the interplay of resources, administrative concerns, and humanities in responding to climate change and socioeconomic calamities (Mohammed 2013; Lin et al. 2018; Mustafa and Ismail 2019; Saleh and Ahmed 2021).

2.4 LULC classification

LULC Classification is the process of appointing land cover classes to pixels and categorize them. For instance, water, urban lands, forests, horticulture, vegetation lands, mountains, and highlands (Rajendran et al., 2020).

The best method for classifying land cover is a remote sensing data classification process (Richards, 1993). The classification workflow divides the pixels in a picture into various classes using supervised or unsupervised techniques (Richards, 1993). Can execute a supervised classification using training data provided and a classification method of maximum likelihood, minimum distance, Mahalanobis distance, Spectral Angle Mapper (SAM), etc., or can perform an unsupervised classification without training data. ENVI (Environment for Visualizing Images) is used to classify the study area. Geographic information systems provide a powerful tool for manipulation in the detection of land cover features.

Unsupervised classification and supervised classification are the two main types of classification processes. Table 2.1 lists the key differences between supervised and unsupervised classification methods. The primary tool for obtaining quantitative data from remotely sensed image data is supervised classification (Richards, 1993). In supervised classification, the training examples could be selected, and the image could be categorised in accordance with the samples that have been selected. Because they will influence which class each pixel in the final image inherits, the training samples are essential. The three steps that could be taken when running a supervised classification are shown in figure 2.1.

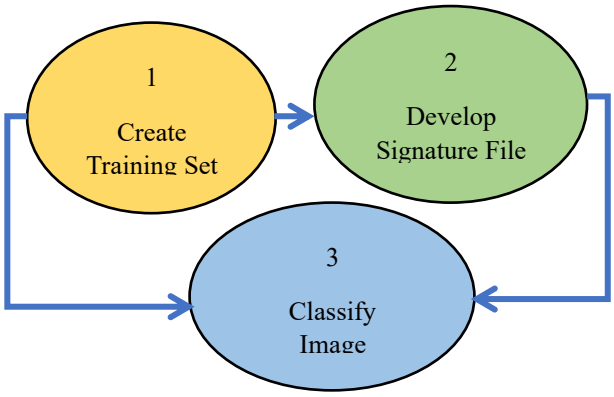

Figure 2.1 The required steps that could be taken when running a supervised classification (Richards, 1993).

Table 2.1 The main distinctions between supervised and unsupervised techniques for classifying land use and land cover (Richards, 1993).

Aspect	Supervised Classification	Unsupervised Classification
Definition	Classification guided by known training samples	Classification without predefined training data
Training Data	Requires labeled training data for each class	No labeled training data required
Process	Involves training the classifier using labeled samples	Uses clustering algorithms to group pixels
User Involvement	Requires user to select training samples	Minimal user intervention during classification
Class Information	Prior knowledge of class identities is needed	Classes are discovered from data patterns
Accuracy Assessment	Often results in higher accuracy due to training	May have lower accuracy due to lack of training
Applicability	Effective for identifying specific classes	Suitable for exploratory data analysis
Flexibility	Less flexible, as predefined classes are used	More flexible, as classes are generated dynamically
Complexity	Potentially more complex due to training process	Generally simpler as it relies on clustering

By using this technique, the analyst can construct representative parameters for each class of interest using a sufficient number of known pixels. Training is the name of this stage. The classifier is used to assign labels to all the picture pixels in accordance with the trained parameters. Maximum Likelihood Classification (MLC), which makes the assumption that each spectral class can be characterized by a multivariate normal distribution, is the most widely used supervised classification technique. As a result, MLC can recognize those extended classes by utilizing both the mean vectors and the multivariate spreads of each class. However, the accuracy of the mean vector and the covariance matrix estimates for each spectral class of data is necessary for MLC to be effective (Richards, 1993).

Additionally, it is predicated on the idea that classes are distributed immorally in multivariate space. We are unable to produce reliable results when the distribution of the classes is multimodal. Unsupervised classification is a different type of classification. In order to classify image data, a clustering method is mostly used, and no human understanding of the classes is necessary (Richards, 1993). The number and position of the unimodal spectral classes can be found using these approaches. The migrating mean clustering classifier is one of the most often used unsupervised classification methods (MMC). According to Richards (1993), this approach is predicated on labelling each pixel with unidentified cluster centres before moving from one cluster centre to another in a way that results in the SSE measure of the prior section being reduced.

In order to identify data about the earth's surface and environment, remote sensing image categorization is necessary. The classification technique identifies the information about the object that corresponds to the image and extracts the essential data about that object (Breiman, 2001) supervised classification and unsupervised classification are the two general categories

used to categorise remote sensing image categorization. We employ supervised categorization in this work.

2.5 Accuracy Assessment

The accuracy assessment method determines how closely the findings match the observed values. The accuracy valuation process involves constructing numerous points from the classified map, comparing their locations, and fitting coordinates from the original photos to positions determined through earth's reality information (Hussain and Karuppannan, 2021). In this study, these points were selected based on random sampling. It should be noted that factors used in classifier training were not taken into account for precise valuation. Fifty points were created as a result, and they were taken into account for creating the error matrix for accuracy assessment. The historical LULC, such as estuaries, croplands, and water bodies, were made possible because of Google Earth information. LU classes were enhanced and identified using a high-quality Google Earth map.

2.6 Change Detection

According to Green et al. (1994), change detection compares the spatial representation of two locations in time while controlling any variances brought on by variations in the variables of interest. Improved resource management and utilisation are possible because of the ability to accurately and quickly detect changes in the earth's surface features (Lu et al. 2004). This capability also paves the way for a deeper comprehension of the relationships and interactions between natural and human activities. Geographic data, typically in digital formats like satellite imagery, analogue format (previous aerial photographs), and vector format (maps), is the most popular sort of data used to detect changes (Singh 1989).

Numerous digital algorithms and approaches for analysing and identifying LU and LC changes have been created and tested in recent decades as a result of the accessibility of substantial archival data sets (Dewidar 2004). These techniques and procedures have undergone in-depth analysis, and excellent summaries and descriptions have been provided (Haque and Basak 2017). It is essential to choose the appropriate change detection method in order to deliver reliable results since it is highly influenced by the temporal, geographical, spectral, and thematic resolutions of remotely sensed data. Unsupervised classification techniques (iterative self-organizing data) include the Affinity Propagation (AP) cluster method, fuzzy c-means algorithms, K-means algorithms, and ISODATA (Maxwell et al. 2018; Camps-Valls et al. 2011).

Numerous studies on LU and LC modelling have been carried out as a result, comparing machine learning algorithms and other machine learning methodologies (Talukdar et al. 2020; Camargo et al. 2019). Additionally, research has been done to select the most suitable and accurate machine-learning classifier among the numerous LULC mapping algorithms (Camargo et al. 2019; Jamali 2019). In this research, the spatio-temporal changes that have occurred have been explored and identified using the GIS-based change detection methodology, which integrates GIS and the RS method (Lu et al. 2004). This method has been chosen to be employed as it allows for the incorporation of several data sources with various data accuracies and formats for long-period periods into LULC change detection (Lu et al. 2004). The method aids in the analysis of the LULC changes' direction, pace, and spatial distribution (Weng 2002).

2.7 Spectral Drought Indices

Since drought is a frequently expected catastrophe that is challenging to identify (counting its beginning, extent, strength, and scope), predict, and manage within the larger environment (Gaznayee et al., 2019; Mohammed and Scholz, 2019),

it has adverse, profound effects on the social, natural, and economic circumstances of the area that is impacted. Due to low average precipitation, a deficiency of natural water sources, high evapotranspiration rates, low water use, a combination of these factors, or both, water scarcity is frequently linked to drought (Mohammed and Scholz, 2017). Additional climatic factors considered essential in determining how often droughts occur include high temperatures, low air humidity, strong winds, timing and precipitation patterns (especially in cultivated growing periods), severity, and extent (Mohammed and Scholz, 2017; 2019). Currently, as countries work to improve modification and adaptation policies, the drought and climate variability effects on water resources have garnered more attention (Mohammed and Scholz, 2017b). According to Lee et al. (2017), water stress, which can be caused by high evapotranspiration rates, excessive water use, or a combination of these factors, is believed to be the second-most important factor in the hydrologic budget after precipitation. Understanding the spatio-temporal pattern of drought is essential because it poses severe risks to people and the environment (Mohammed and Scholz, 2019). Different portions of the globe are predicted to experience more recurrent and severe droughts due to climate change (Hussain et al., 2022). Once there is a persistent deficiency in rainfall, a climatological drought occurs (Mohammed and Scholz, 2017a). A drought in agriculture is defined by a lack of precipitation, which leads to dwindling soil moisture and inadequate vegetation (Mohammed and Scholz, 2017a).

Iraq has been extensively researched and is referred to in the literature as the northern regions of Mesopotamia or the fertile crescent (Gaznayee & Al-Quraishi, 2019; Gaznayee et al., 2019). Over the past few decades, the northern region of Iraq and other areas have experienced a severe drought marked by a sharp decline in precipitation rates (Al-Quraishi et al., 2019; Mustafa, 2020). Drought can have multiple consequences, including groundwater depletion, lake

and reservoir depletion, water shortages, and decreased availability of field crops and feed (Zakaria et. al., 2013; Mustafa, 2020). In relation to agriculture, the northern high-precipitation region is dominated by vegetable production and fruit orchards, while wheat fields dominate the intermediate-precipitation region and in low-precipitation areas, barley is the primary crop. Depending on precipitation, barley and winter wheat are harvested in the late spring (April–June) after they are planted in the fall (October-November) (Schnepf, 2004; Eklund and Pilesjo, 2012; Zakaria et al., 2013).

The drought progression is divided into two stages: Firstly, a meteorological drought is defined as a long period without rain that signals the start of a drought event. Second, a lack of rainfall reduces available soil water and vegetation cover, resulting in agricultural drought (Almamalachy et al., 2020). Geographic information systems (GIS) and (RS) are becoming more popular for drought detection (Chopra, 2006). In its current state of development, RS technology can help with disaster prediction, mitigation, and monitoring. The latter is done successfully worldwide, with indices resulting from optical RS figures.

Contrarily, drought has been extensively studied and mapped using spectral drought indices (Chopra, 2006; Gaznayee and Al-Quraishi, 2019). Whether a researcher is interested in agriculture, meteorology, or hydrology, they can use data from various satellites for various projects. These data make it possible for us to more clearly understand the effects of drought across a wider region (Menon and Bhavana, 2016) compared to slower traditional methods.

Geo-information technology (GIS, RS, and GPS), which integrates the acquisition, modelling, examination, and managing of spatially distributed data, is regarded as a modern discipline of the sciences (Al-Quraishi and Negm, 2019; Mustafa and Ismail, 2019). Vegetation is the first component of the environment that is impacted by drought. The land surface system is crucial for tying together environmental elements such as water, soil, air, and additional ecological components (Foley et al., 2000).

RS data may be the only information source for drought monitoring in locations with few sampling gauges (Julien and Sobrino 2010; Juliev et al. 2019; Sameer et al. 2021, 2023). Globally, drought intensity, duration, and impact have all been measured using satellite-based drought indices (Goward et al. 2002; Gaznayee and Al-Quraishi 2019; Hussain et al. 2020a; Dibaba et al. 2020; Gaznayee et al. 2021; Mohammed and Sayl 2021).

The NDVI, which deals with the robustness of vegetation and has a strong link with green biomass, an indicator of healthy vegetation or crops, was calculated mathematically utilising spectral bands inside the satellite picture (Saleh and Ahmed, 2021; Hussain et al., 2020b). The NDVI creates an adaptable way to calculate plants' amount, value, and growth by relating near-infrared and red colour spectral information (Yesuph and Dagnew 2019). High-resolution satellites such as the Landsat series, the Sentinel series, and various on-board sensors are currently available to estimate the vegetation index at local (Mustafa 2020) and universal levels (Dibaba et al. 2020; Hussien and Karuppannan 2022; Mohammed et al. 2022).

The VCI was created to separate ecological and weather-related signals in the NDVI. Gaznayee et al. (2021) results highlight relationships with some ecological variables and demonstrate the VCI's ability to detect characteristics of droughts, providing crucial data to decision-makers in the environmental and economic sectors. Furthermore, LST measures the energy balance of the earth's surface, providing vital information about the physical properties and climate of the planet (Aryan et al. 2018; Assaf et al. 2021).

Gaznayee et al. (2022) reported a negative correlation between LST and NDVI, as an increase in LST was observed at several scales due to changes in vegetation cover and soil moisture, indicating that surface temperatures can rise rapidly with water stress. Recent research has described the correlation between NDVI

and LST (Sun et al. 2010; Mohammed and Sayl 2020; Gaznayee et al. 2022; Sayl et al. 2022), which is one of many factors that negatively affect vegetation dynamics, as an essential element.

2.8 Summary

Based upon the previous review of literature, arise the need to conduet a study uses RS and GIS to prepare LULC maps and calculate various spectral indices, including the Normalized Difference Vegetation Index (NDVI), the Vegetation Condition Index (VCI), the Soil Adjusted Vegetation Index (SAVI), the Normalized Difference Water Index (NDWI) and Normalized Difference Build-up (NDBI) in order to detect changes in LULC and correlate these changes with Land Surface Temperature (LST). This integrated approach allows the present study to gain more understanding of complex relationships between LULC, vegetation, and draught.

CHAPTER THREE

MATERIALS AND METHODS

3.1 The Study Area

The watershed of Diyala River Basin is typically used as example for semi-arid and arid climates (Al-Faraj and Scholz, 2014). At Lake Derbendikhan in the Sulaymaniyah Governorate of northern Iraq, the Tangro, Wand, and Sirwan rivers converge to form the Tangro River, the fifth tributary of the Tigris River. The river begins in the Zagros Mountains and flows through Iran and Iraq for approximately 574 kilometers before entering the Tigris River south of Baghdad, Iraq. The entire area is roughly 32975.6259 km^2, of which 46% is in Iraq and the rest in Iran. Figure (3.1) illustrates the location of the Diyala River Basin, which is located between latitudes 33°12'00″ and 35°47'00″ E and longitudes 44°18'00″ and 47°58'00″ N.

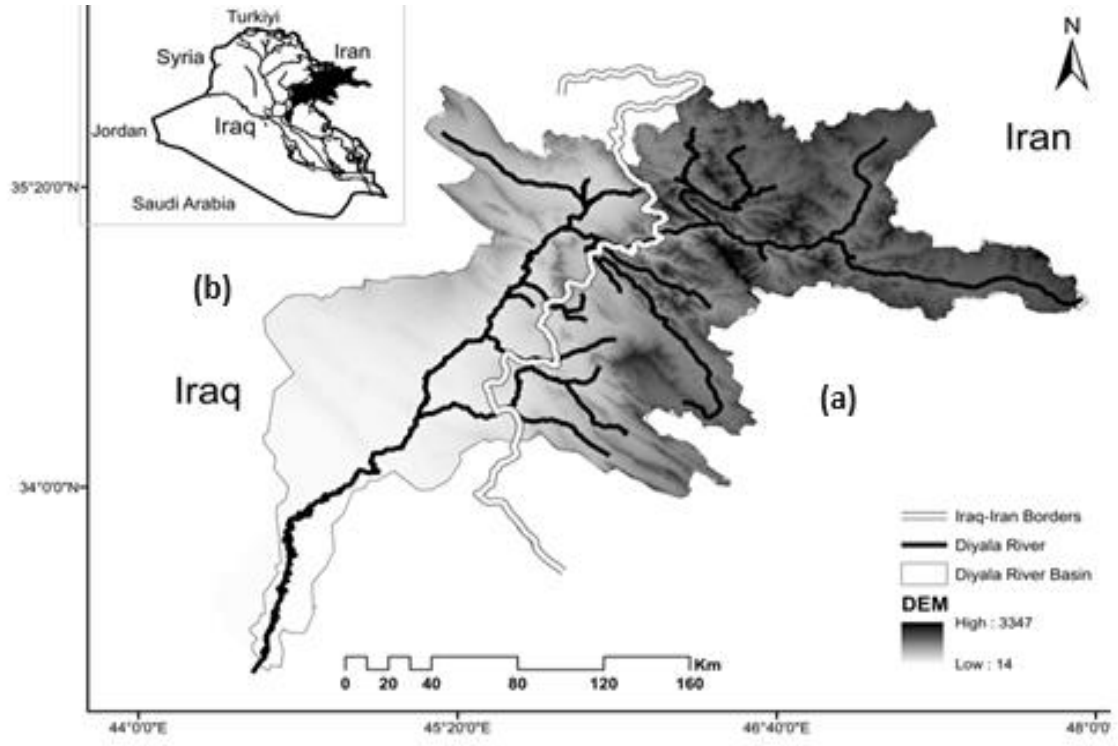

Fig. 3.1 The Diyala River Basin's hydrographic system can be found: (a) in iran (b) in Iraq.(https://earthexplorer.usgs.gov).

Derbendikhan (35°06′46″N 45°42′23″E), considered among the largest dams in Iraq, manages the flow of the river. As shown in the figure 3.2 the Derbendikan is an earth rockfill dam that was built in 1961 and serves several functions, including flood control, hydropower generation, and irrigation. About 20% of its 16,750 km^2 is in Iraq, and the remaining 80% is in Iran (Naqi et al., 2021). The Derbendkhan Reservoir can hold 3.5 million cubic meters of water in total (MCM). Upstream, the Diyala River has a length of about 217 kilometers.

Fig. 3.2 Derbendikan earth rockfill dam.

As shown in the figure 3.3 the Hemrin (34°06′52″N 44°58′04″E), earthfill with clay core and gravel shells dam in DRB, is the second dam. About 120 kilometers to the east of Baghdad City, in the middle of the Diyala River, Hemrin was constructed in 1981 (Al-Faraj and Scholz, 2015).

Fig. 3.3 Hemrin earthfill with clay care and gravel shells dam.

3.2.1 Spatial and Temporal Data

Figure (3.1) shows satellite images that were downloaded from the USGS (the United States Geological Survey) (https://earthexplorer.usgs.gov) (accessed September 20, 2022) and included the Digital Elevation Model with a spatial resolution of 30 meters. The basin was enclosed via Landsat 8,9 (OLI) and TIRS imagery with path/row = 167/36, 168/37, having 30 m spatial resolution and nine spectral bands. The Landsat images were downloaded for four periods, which are the years 2013, 2016, 2019, and 2022. Landsat combinations, Google Earth, and ground control points (GPs) were gathered by the Global Positioning System (GPS) for the classification of Landsat photos and accuracy evaluation as given in Table (3.1) downloaded from (https://earthexplorer.usgs.gov).

Table (3.1) Data gathered from Earth observation pictures for the Diyala River Basin (https://earthexplorer.usgs.gov).

S. No.	Satellite/Sensor	Date	Path/Row	Spatial Resolution	Spectral Resolution	Band Used
1	Landsat 8(OLI/TIRS)	7 April 2013	167/36 168/37	30	Multispectral (1-7,9 bands)	1-,7 and 9
				100	Band 10	10
2	Landsat 8 (OLI/TIRS)	6 April 2016	167/36 168/37	30	Multispectral (1-7,9 bands)	1-7, and 9
				100	Band 10	10
3	Landsat 8 (OLI/TIRS)	24 May 2019	167/36 168/37	30	Multispectral (1-7,9 bands)	1-,7 and 9
				100	Band 10	10
4	Landsat 8,9(OLI/TIRS)	23 April 2022	167/36 168/37	30	Multispectral (1-7,9 bands)	1-,7 and 9
				100	Band 10	10

Note: In 2019, photos in April were not selected due to clouds and lack of clarity in aerial photos in this month.

3.2.2 Meteorological Data

Climatic data such as minimum and maximum air temperatures and precipitation data for the study period of DRB have been obtained from the National Aeronautics and Space Administration (NASA) (http://power.larc.nasa.gov) (accessed on November 21, 2022).

3.3 Data Analysis Softweares

1. **ArcGIS 10.8**: ArcGIS 10.8 was used to create LU and LC maps and image classification and calculate NDVI, VCI, NDBI, SAVI and NDWI.

2. **Google Earth:** Google Earth was utilized to check the classification LU/LC and calculate the accuracy assessment.

3. **Microsoft Excel 2021**: The Excel 2021 programme was used to arrange the values of the tables that were obtained from ArcGIS 10.8, and to draw the relationship between indicators, such as the relationship between NDVI and LST.

3.4 Classification Procedures

3.4.1 Classical Maximum Likelihood Classifier

Maximum likelihood classification was applied to categorise each pixel. Although it is recommended to perform at least 20 trials when classifying a picture using a map with less than three classes, this study used at least 30 reference samples for each class. The reference sites for 2013, 2016, 2019, and 2022 on Google Earth were taken into consideration. There are numerous steps in the overall process of classifying images. The initial step is to choose training locations.

Using the processed images as a guide, training locations were sampled using the polygon technique, which allowed for the sketching of polygons for a particular spectral class. During the process, various band arrangements, picture enhancements, and colour configurations were used to distinguish between and comprehend the surface structures of the photographs. Every band represents a data set file for a certain electromagnetic field ratio used to determine the study features. The band groupings were chosen based on their applicability. The samples extracted signs were estimated using the histogram approach, and numerous trials were conducted until the desired unimodal distribution was achieved. The same-class signs were then combined by selecting all the signs from each class. Additionally, the training data set is used to generate class signatures and the whole-picture classification. A compound signature was used in the supervised image classification maximum likelihood map to map the LU and LC. The LU and LC class change portion (CP) and fraction of illustrative change (FC) in the LU and LC class area can be estimated by applying the following equations:

$$\mathrm{CP}\left(\mathrm{Km}^2\right) = \mathrm{OA} - \mathrm{EA} \qquad 3.1$$

$$FC\ (\%) = \frac{OA - EA}{A} \times 100 \qquad 3.2$$

In which OA is the last year extent (km^2), EA is the first year extent (km^2), and A is the overall area of the basin (km^2).

3.4.2 Accuracy Assessment

Data on LU and LC features, and other types of thematic data essential to GIS analysis, are mostly derived via RS. To assess the distribution of LC and to update current geospatial information, aerial, and Landsat satellite imageries are also commonly used. The significance of RS in GIS has increased dramatically with the development of RS technologies and image processing software (Mahdi and Mohammed, 2022). While geospatial processes are now more efficient and powerful as a result of the greater use of RS data and technology, the complexity has also raised the likelihood of error. Earlier, studies on picture categorization did not place a high premium on accuracy evaluation. Yet, accuracy assessment has become an extremely important process due to the accelerated potential for error given by digital photography (Congalton and Green, 2019)

A crucial stage in the processing of data from RS could be accuracy assessment or validation. It increases the value of the upcoming information for the user. The quality of the information must be known in order for geodata to be used profitably. The overall accuracy of the categorised image is evaluated by comparing the classification of each pixel to the clear land cover conditions derived from the associated ground truth data. The accuracy of the producer, which may serve as a barometer for how well real-world land cover categories may be identified, is used to measure errors of omission. According to Congalton (1991), Jensen (2005), and Campbell (2007), the chance that a classed pixel on each map corresponds to the actual class on the ground or real-world location is

known as user accuracy (UA). The error matrix and kappa coefficient have become the accepted metrics for assessing the precision of image classification.

These points were selected based on random sampling. It should be noted that factors used in classifier training were not taken into account for precise valuation. Fifty points were created as a result, and they were taken into account for creating the accuracy assessment error matrix. The historical LULC, such as estuaries, croplands, and water bodies, was made possible because of Google Earth information. LU classes were enhanced and identified using a high-quality Google Earth map. Considering the overall accuracy, user and producer accuracy, and the error array, the Kappa Index (KI) was estimated. KI typically ranges from 0 to 1, and values below 0.4 denote low agreement; between 0.4 and 0.8, moderate agreement; and over 0.8, robust arrangement (Viera and Garrett 2005) as shown in table (3.2).

Table (3.2) Statistical measurements to evaluate the intelligent accuracy of a category (Viera and Garrett, 2005).

no.	kappa statistic	power of agreement
1	0 >	Less than chance agreement
2	0.20–0.01	Slight agreement
3	0.40 –0.21	Fair agreement
4	0.60–0.41	Moderate agreement
5	0.80–0.61	Substantial agreement
6	1–0.81	Almost perfect agreement

The overall accuracy is computed by dividing the total number of pixels by the total number of correctly categorised pixels. Pixels examined The Kappa coefficient is an agreement metric. The proportion reflects the classification's degree of accuracy (Congedo, 2021). As a result, concentrated on general change rather than land cover-specific changes.

An error matrix and Kappa coefficient, including user classification and a reference image, were used to assess accuracy (Tembo and Volk, 2022). An error matrix is a very efficient way to convey the accuracy of thematic maps since it

provides a simple way to identify the specific accuracies of each class as well as both inclusion and exclusion errors (commission and omission errors). The overall accuracy, user's accuracy, producer's accuracy, and Kappa coefficient were calculated using the following equations (Al-Saady et al., 2015; Dibaba et al., 2020):

$$OA = \frac{(\text{total number of classified pixels (daigonal)})}{(\text{total number of reference pixels})} \times 100 \quad 3.3$$

$$UA = \frac{(\text{number of correct classified pixels for each classes })}{(\text{total number of pixels in the classif ied image})} \times 100 \quad 3.4$$

$$PA = \frac{(\text{number of correct pixel in the classified map for each classes })}{(\text{total number of reference pixels(Google earth)})} \times 100 \quad 3.5$$

$$KI\% = \frac{(\text{total no. of (diagonal} \times \text{reference)} - (\sum(\text{user} \times \text{procdure}))}{(\text{total no.of reference})^2 - (\sum(\text{user} \times \text{procdure})} \times 100 \quad 3.6$$

Producer and user accuracy and the whole Kappa index of the agreement were calculated, depending on the error matrix. The transition error matrix of the LU and LC denotes the LU and LC change during 2013, 2016, 2019, and 2022 in this study, for example. The transition matrix is defined by (Daba and You, 2022):

$$A_t = \begin{bmatrix} A_{t_{11}} & A_{t_{12}} \ldots\ldots\ldots & A_{t_{1j}} \\ A_{t_{21}} & A_{t_{22}} \ldots\ldots\ldots & A_{t_{2j}} \\ \ldots\ldots\ldots\ldots\ldots\ldots\ldots\ldots & & \\ A_{t_{i1}} & A_{t_{i2}} \ldots\ldots\ldots & A_{t_{ij}} \end{bmatrix} \quad 3.7$$

where A_{ij} = the area in transition from land i to land j, and each element in the transition matrix is categorised assuming A_{ij} is non-negative and The quantification of the changing aspects of modification during the time frame was then explored by computing the zone of specific classification for each time frame (every year 2013, 2016, 2019, and 2022) after evaluating its produced LU and LC maps accuracy between 2013 and 2022.

3.4.3 Change Detection

To create the LU and LC images for 2013, 2016, 2019, and 2022, ArcMap 10.8 (ESRI, 2020) was used. First, the land cover categorizations were accomplished, and the LU and LC classifications were assessed. Then LU and LC investigations and degrees of change were considered. The following equations are used to determine the total LU and LC between two periods (Mahdi and Mohammed, 2022):

$$\text{Overall LU and LC change} = \text{Area of the last year} - \text{Area of the first year} \quad (3.8)$$

$$\text{Ratio of LU and LC change} = \frac{\text{Overall LU and LC change}}{\text{Full basin area}} \times 100 \quad (3.9)$$

A matrix of LU and LC was established for 2013, 2016, 2019, and 2022 using the ArcMap environment to test the LU and LC inter-classification changes and analyse the catchment practice in LU and LC changes. This array calculated the difference in the region (growth or reduction), stability, and change between the LU and LC classes.

3.4.4 Normalized difference vegetation index

Normalized Difference Vegetation Index (NDVI) is the most generally applied vegetation cover index. NDVI is used to investigate and evaluate plant density and health changes. As shown in table (3.3).

The following equations are used to estimate NDVI (Hussain and Karuppannan, 2021):

$$NDVI = \frac{(NIR - R)}{(NIR + R)} \quad (3.10)$$

in which

NIR = near-infrared (0.85−0.88 μm).

R = red (0.64−0.67 μm).

$$NDVI = \frac{(Band\ 5 - Band\ 4)}{(Band\ 5 + Band\ 4)} \quad 3.11$$

Table (3.3) Statistical measurements to calculate Normalized Difference Vegetation Index (Hussain and Karuppannan, 2021).

no.	NDVI Value	NDVI Classes
1	-1 – -0.1	water bodies
2	- 0.11 – 0.1	Urban land
3	0.11 – 0.2	Barren rocks, sand, or snow
4	0.21 – 0.5	Grasslands
5	0.51 – 1	Dense foliage

3.4.5 Land Surface Temperature

Land surface temperature (LST) was derived by applying the following stages:

1. convert thermal data to radiance using the following equation: (Sun et al., 2010).

$$L_\lambda = ML \times Q_{cal} + AL \quad 3.12$$

2. Converting L_λ to Brightness Temperature (BT):

$$BT = \frac{K_2}{\ln\left(\frac{K_1}{L_\lambda}\right) + 1} - 273.15 \quad 3.13$$

3. Calculating NDVI

$$NDVI = \frac{(Band\ 5 - Band\ 4)}{(Band\ 5 + Band\ 4)} \quad 3.14$$

4. Calculating the vegetation proportion (P_v)

$$P_V = \left(\frac{NDVI - NDVI_{min}}{NDVI_{max} - NDVI_{min}}\right)^2 \quad 3.15$$

5. Calculate Emissivity ε

$$\varepsilon = 0.004 \times P_V + 0.986 \quad 3.16$$

6. Calculating the LST

In the last step, the following equation could be applied to produce the surface temperature (Hussain and Karuppannan, 2021).

$$LST = \frac{BT}{1+(\frac{0.00115 \times BT}{1.4388} \times \ln(\varepsilon))} \quad 3.17$$

It is important to understand that the LST is not the same as the air temperature.

in which L_λ = (the top of the atmospheric) TOA

ML= RADIANCE_MULT_BAND_10

Q_{cal} = corresponds to band 10;

AL = RADIANCE_ADD_BAND

K1 = K1_CONSTANT_BAND 10

K2 = K2_CONSTANT_BAND_10

3.4.6 Vegetation Condition Index

The vegetative condition index (VCI) was created to separate the biological components of the NDVI from the component that is linked to the weather. The following equation can be used to estimate VCI (Gaznayee et al., 2021).

$$VCI = \frac{NDVI - NDVI_{min}}{NDVI_{max} - NDVI_{min}} \times 100 \quad 3.18$$

where NDVI stands for the NDVI value for the current month, and $NDVI_{min}$ and $NDVI_{max}$ stand for, respectively, the lowest and highest values of the NDVI in the observation.

The VCI index relates recent NDVI values to values recorded during the same period in past years in a specific pixel since it has often been recommended based

on the relative NDVI fluctuation with regard to the minimum historical NDVI value. Several studies used the VCI as a technique to measure the severity of the drought; however, the only VCI values provided insufficiently detailed assessments of the situation (Gaznayee et al., 2021). Table 3.4 shows the VCI values and the corresponding drought categories.

Table 3.4 Classification of the Vegetation Condition Index (VCI) values in relation to drought (Quated from Gaznayee et al., 2021).

Classification	VCI Values
Extreme Drought	$10 \geq$ VCI
Severe Drought	$10 <$ VCI ≤ 20
Moderate Drought	$20 <$ VCI ≤ 30
Mild Drought	$30 <$ VCI ≤ 40
No Drought	VCI > 40

3.4.7 Normalized Difference Water Index

An indicator of water body change monitoring that uses the green and NIR bands is the Normalized Difference Water Index (NDWI). That can be expressed by (Gaznayee and Al-Quraishi, 2020):

$$NDWI = \frac{Green - NIR}{Green + NIR} \qquad 3.19$$

In which Green is the green band (B3), (0.53-0.59 μm), NDWI stands for the normalized differential water index, and NIR is the near-infrared band (B5), (0.85–0.88 μm).

A body of water has a high absorption capacity and little Infrared and Visible rays radiation. Using a threshold value, the water body can be divided into surfaces with detectable water (NDWI figures greater than or equal to 0.3) and those without discernible water, according to McFeeters (1996). In the current study,

the size of water bodies like Derbendikan Lake (DLK) and Hemrin Lake (HLK) was estimated using the NDWI, and the ArcGIS software was used to classify the NDWI fraction images.

3.4.8 Normalized Difference Built-up Index

Compared to other surface features, built-up lands have higher reflectance. NDBI is useful to map urban built-up areas, which is expressed as follows (Zha, 2003).

$$NDBI=\frac{(MIR-NIR)}{(MIR+NIR)} \quad 3.20$$

where NIR is near infrared reflectance, which is (1.57–1.65 μm), band 5; MIR is middle infrared reflectance, which is (0.88–0.88 μm) band 6. NDBI values range from -1 to 1. The greater the NDBI is, the higher the proportion of built-up land is, and the larger areas of construction land there are.

3.4.9 Soil Adjusted Vegetation Index

In an effort to enhance the NDVI, Huete (1988) created a vegetation index that took into consideration the differences in red and near-infrared extinction across the vegetation canopy. The index is a transformation approach that reduces soil brightness effects from spectral vegetation indices using red and near-infrared (NIR) wavelengths. The SAVI is defined by:

$$SAVI=\frac{(1+L)(NIR - Red)}{(NIR + Red + L)} \quad 3.21$$

where L is a canopy background adjustment factor. An L value of 0.5 in reflectance space was found to minimize soil brightness variations and eliminate the need for additional calibration for different soils. The transformation was found to nearly eliminate soil-induced variations in vegetation indices (Huete, 1988).

3.5 Research Methodology

Aerial photographs from Landsat 8,9 for the years 2013, 2016, 2019, and 2022 were used to draw LU and LC maps and calculate the quantities of the five types: water bodies, urban areas, bare lands, vegetation land, and palm trees. The NDVI was also calculated and mapped, and the LST values were calculated and linked to a relationship to determine the strength of the correlation that occurs between them. The VCI was also calculated to determine the incidence of drought in the study area during the years of the study, and the NDBI was calculated to determine the expansion of urban areas throughout the study period.

While from the year 2013 to 2022 These images were used to measure the water bodies in Lake Derbendikan and Hemrin using NDWI, and the VCI was also calculated during this period to determine drought conditions for a period of 10 years, as shown in figure (3.4).

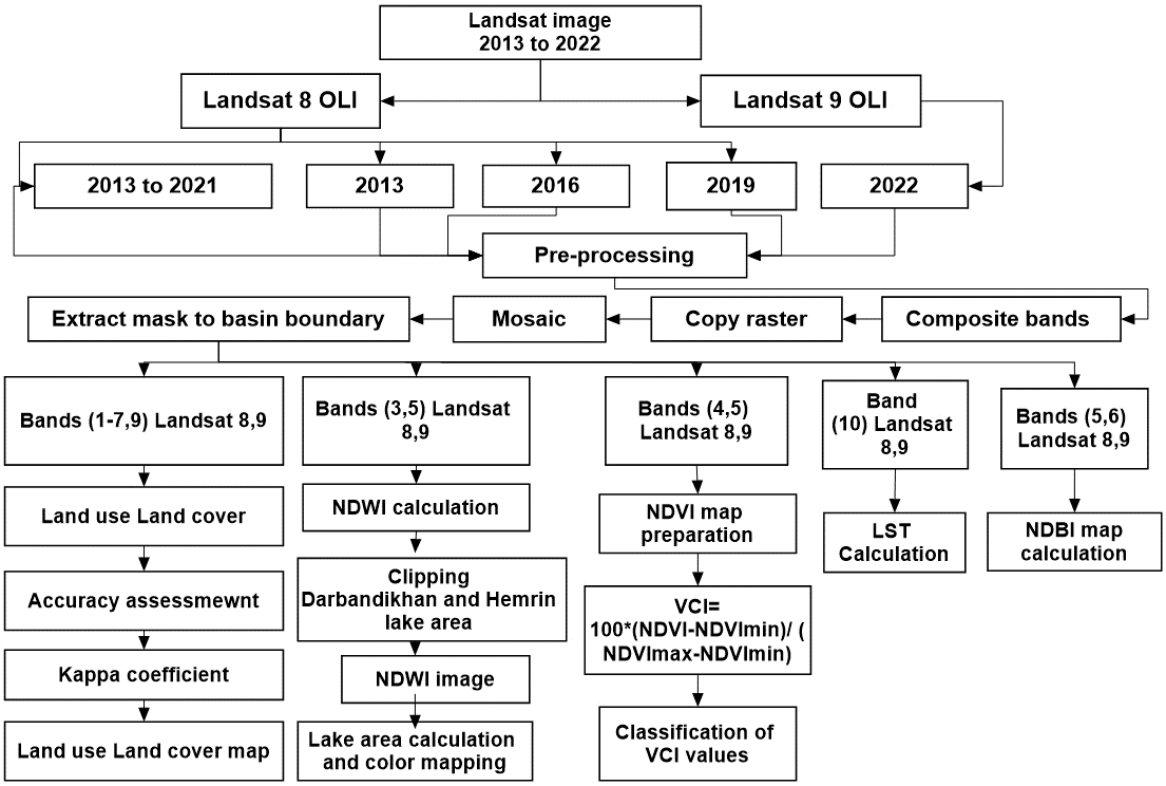

Figure (3.4) Adopted methodology for assessing the land use and land cover alteration on the Diyala River Basin.

CHAPTER FOUR

RESULTS AND DISCUSSION

4.1 Land use/Land Cover Alterations

The change of LULC has been considered an essential focus that needs to be addressed in the environmental variation study and urban expansion and development. In order to the LULC classes in the (DRB), Landsat images for the periods 2013, 2016, 2019, and 2022 were used as shown in Figure 4.1. The basin area was comprised of different land types, which are water bodies, urban lands, barren lands, vegetation areas, and palm lands. The classification of LULC was engaged along with an investigation analysis using Google earth. The main LULC classes in the basin were the vegetation areas that covered about 76.64%, 57.36%, 63.63%, and 68.00% during 2013, 2016, 2019, and 2022, in that order as shown in Table 4.1 and Figure 4.1. Then came the deserted areas and cities, which increased by 381.57 km^2 (1.16%) and 2730.77 km^2 (8.28%) from 2013 to 2022, respectively.

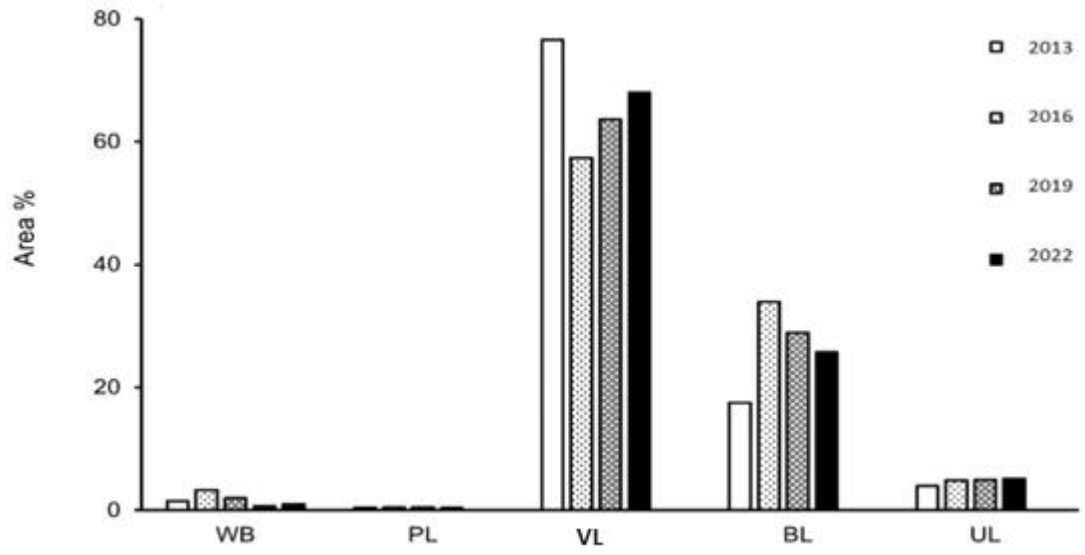

Figure 4.1 Temporal variation of Land use and land cover classes of the Diyala Basin throughout 2013, 2016, 2019, and 2022.

Even though vegetation cover had reduced between 2013 and 2022, there seems to be a positive alteration in the area, with an increase of 6.27% between 2016 and 2019. The water bodies class comprised 501.10 km2 (1.52%) in 2013, but decreased by -274.12 km2 (-0.83%) between 2013 and 2022 (Table 4.1). It has been observed that during the study period, vegetation cover has altered between built-up lands and barren areas. It has been noticed that the bare land has increased during the last decade. In 2013, about 5770.30 km^2 (17.50%) of the basin was covered by bare lands, which increased to 8501.08 km^2 (25.78%) in 2022. Besides, in 2022, the bare land area increased by 8501.08 km^2 (25.78%) (Table 4.1). Still, there was a significant rise in bare land from 2013 to 2016, increasing by 5430.61 km^2 (16.47%). In 2022, the main LU and LC categories were vegetation cover (68%), followed by barren areas (25.78%), and built-up lands (5.09%).

Table 4.1 Land use and land cover (LU//LC) classes area over the study period.

Year	Unit	LU/LC class					Total
		WB[1]	UL[2]	BL[3]	VL[4]	PL[5]	
2013	Km^2	501.1	1295.8	5770.3	25273.9	134.5	32975.6
	%	1.5	3.9	17.5	76.6	0.4	100.0
2016	Km^2	1085.7	1620.0	11200.9	18914.5	154.6	32975.6
	%	3.3	4.9	34	57.4	0.5	100.00
2019	Km^2	662.6	1631.4	9540.6	20983.8	157.2	32975.6
	%	2.0	5.0	28.9	63.6	0.5	100.0
2022	Km^2	227.0	1677.4	8501.1	22421.8	148.3	32975.6
	%	0.7	5.1	25.8	68.0	0.5	100.0
CP	Km^2	-274.1	381.6	2730.8	-2852.0	13.8	0
FC%	%	-0.8	1.2	8.3	-8.7	0.0	0

[1]Water Bodies; [2]Urban Lands; [3]Bare Lands; [4]Vegetation Lands; [5]Plams; CP=Change between 2013 and 2022, FC=Percentage of change.

During the studied period, agricultural lands witnessed the largest decline. The deterioration in soil moisture content of the DRB, which originated due to lower average annual rainfall during the past years, is generally responsible for the decline in agricultural lands.

The expansion or contraction of the region covered by a specific LU or LC class can be denoted by the extent and percentage of the variations recognised. Expansion and contraction of the corresponding LU and LC class's spatial magnitude are usually represented by positive and negative numbers, respectively. The temporal variations of LU and LC in the DRB during the study period are displayed in Figure 4.1. Though the spatial and temporal LU/LC variations in DRB are shown in Figure 4.2, Vegetation cover and built-up lands witnessed continuous growth, although barren lands exhibited a continuous drop. The upper basin portion showed the most growth in agricultural lands, while the lower basin portion showed the greatest growth in urban areas.

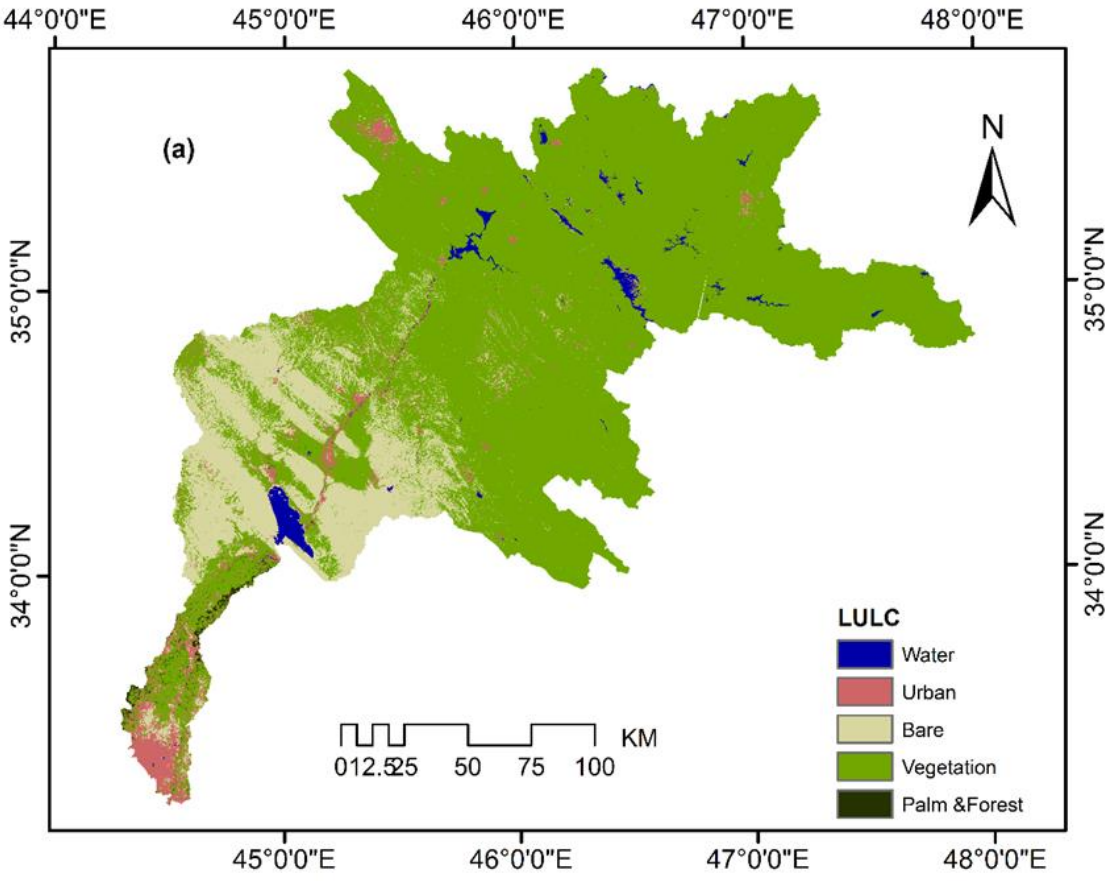

(a):Satiotemporal variations of LULC at 2013.

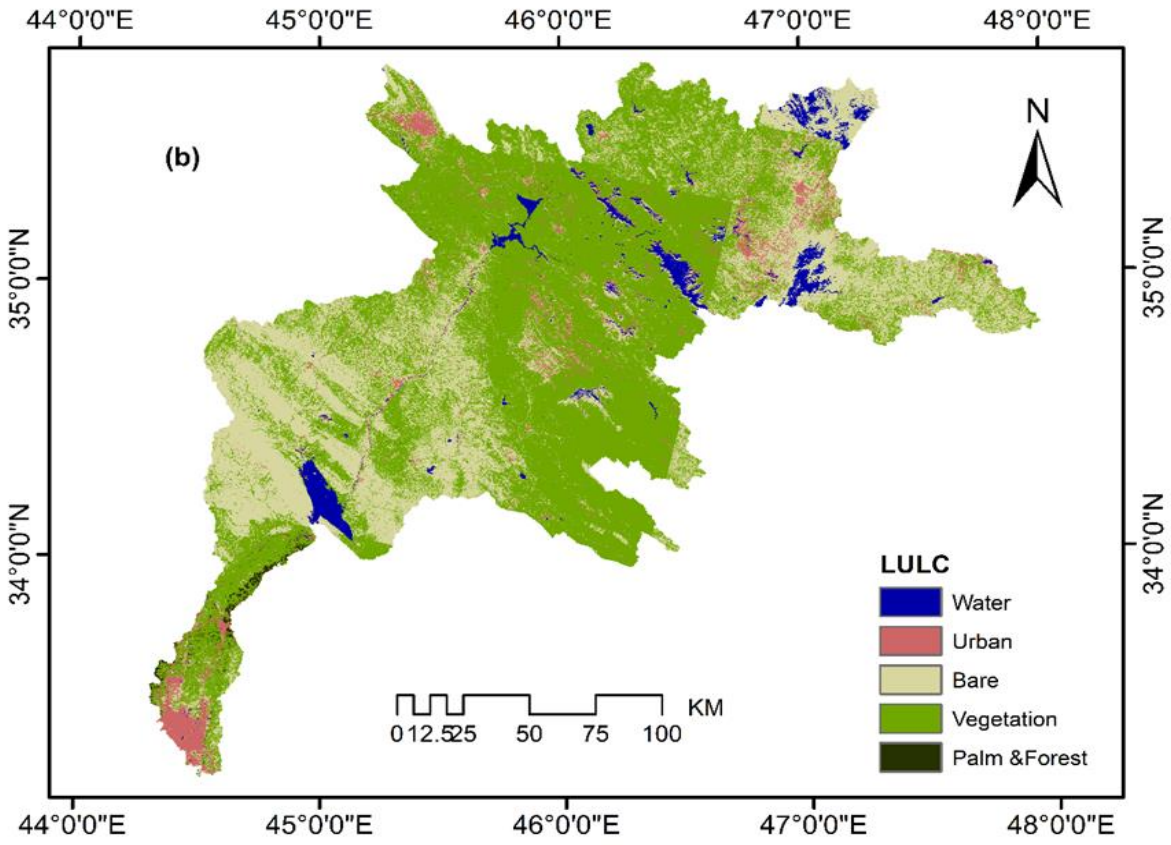

(b):Satiotemporal variations of LULC at 2016.

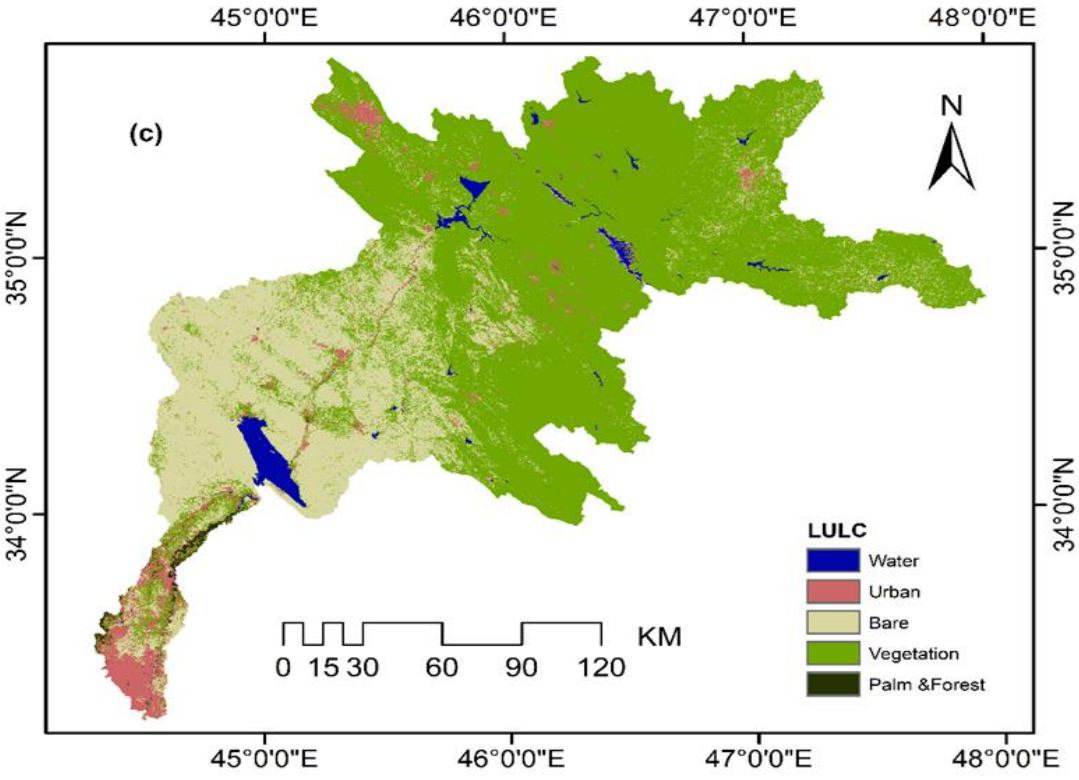

(c):Satiotemporal variations of LULC at 2019.

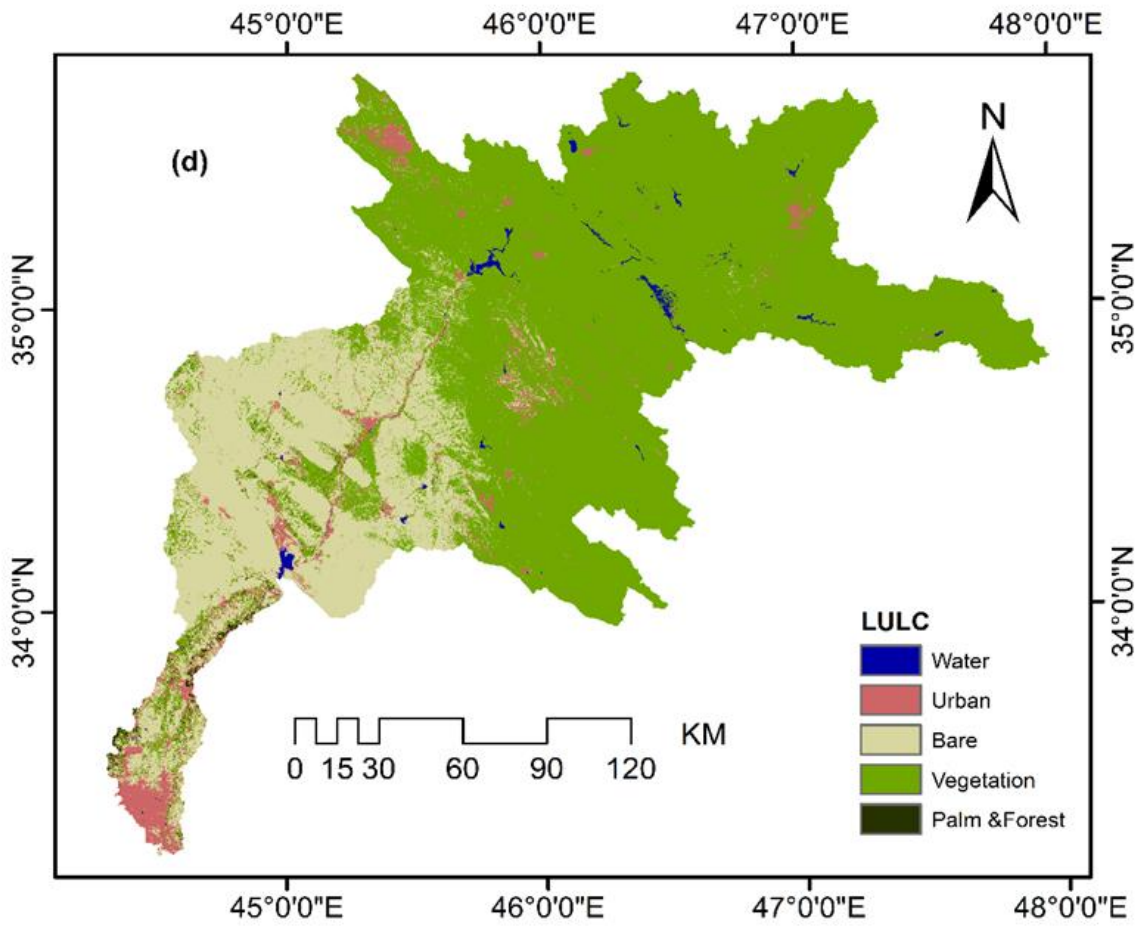

(d):Satiotemporal variations of LULC at 2022.

Figure 4.2 Land use and land cover spatiotemporal alteration for Diyala River Basin over study period.

Based on these findings, it was concluded that population growth resulted in a significant reduction in vegetation cover. Similarly, between 2013 and 2022, a lack of water bodies resulted in an increase in barren areas and a lack of vegetation cover**.**

4.2 Accuracy Evaluation of Land Use and Land Cover

As shown table 4.2 displays the estimation results of the producers' (PA) and users' (UA) accuracy, overall accuracy assessment (OA), and the Kappa coefficient values for different LU/LC classes for the 2013, 2016, 2019, and 2022 years, respectively. The OA and the KI values were 93% and 91.2%, 88. 7% and 85.8%, 89.2 and 86.5%, and 90.2% and 87.7%, respectively. The maximum and

minimum PA values detected for the bare lands, vegetation lands, and palms were in the range of 92.9% to 83.3%, 91. 7% to 73.3%, and 91. 7% to 71.4%, in that order. The corresponding values of UA detected for urban lands, vegetation lands, and palms were in the range of 92.3% to 90.9, 92.3% to 81.8%, and 91.67% to 66. 7%, in that order.

Table 4.2 The estimation of the Kappa coefficient (KI) and overall accuracy (OA) for the water years 2013, 2016, 2019, and 2022.

Year	LU/LC	GCRD[a]					GTH[b]	UA[c]
		WB[1]	UL[2]	BL[3]	VL[4]	PL[5]		
2013	WB[1]	**11**	0	1	0	0	12	91.7
	UL[2]	0	**10**	0	0	1	11	90.9
	BL[3]	0	0	**10**	0	0	10	100
	VL[4]	0	0	1	**11**	0	12	91. 7
	PL[5]	0	0	0	1	**11**	12	91.7
	Total	11	10	12	12	12	**57**	
	PA[d]	100	100	83.3	91.7	91.7		
	OA%	**93**						
	KI%	**91.2**						
Year	LU/LC	GCRD[a]					GTH[b]	UA[c]
		WB[1]	UL[2]	BL[3]	VL[4]	PL[5]		
2016	WB[1]	**9**	0	0	0	0	9	100
	UL[2]	0	**10**	0	0	1	11	90.9
	BL[3]	0	0	**10**	0	0	10	100
	VL[4]	0	0	2	**9**	0	11	81.8
	PL[5]	0	0	0	3	**9**	12	75
	Total	9	10	12	12	10	**53**	
	PA[d]	100	100	83.3	75	90		
	OA	**88.7%**						
	KI	**85.8%**						
Year	LU/LC	GCRD[a]					GTH[b]	UA[c]
		WB[1]	UL[2]	BL[3]	VL[4]	PL[5]		
2019	WB[1]	**12**	0	0	1	0	13	92.3
	UL[2]	0	**12**	0	0	1	13	92.3
	BL[3]	0	0	**13**	0	0	13	100
	VL[4]	0	0	1	**11**	1	13	84.6
	PL[5]	0	0	0	3	**10**	13	76.9
	Total	12	12	14	15	12	**65**	
	PA[d]	100	100	92.9	73.3	71.4		
	OA	**89.2%**						
	KI	**86.5%**						

Table 4.2 :continued

Year	LU/LC	GCRD[a]					GTH[b]	UA[c]
		WB[1]	UL[2]	BL[3]	VL[4]	PL[5]		
2022	WB[1]	**12**	0	0	0	0	12	100
	UL[2]	0	**11**	0	0	1	12	91.7
	BL[3]	0	0	**12**	0	0	12	100
	VL[4]	0	0	1	**12**	0	13	92.3
	PL[5]	0	0	1	3	**8**	12	66.7
	Total	12	11	14	15	9	**61**	
	PA[d]	100	100	85.7	80	88.9		
	OA	**90.2%**						
	KI	**87.7%**						

[1]Water Bodies; [2]Urban Lands; [3]Bare Lands; [4]Vegetation Lands; [5]Plam; [a]Ground Control Reference Data (Google Earth); [b]Ground Truth; [c] Use's accuracy (%); [d] Producer's accuracy (%).

Based on the findings, the KI values showed significant agreement across all examined years.

4.3 Change Detection Matrix

The investigation of the LU/LC alteration supports the determination of how a definite class can move to another one. The LU/LC changing matrixes from 2013 to 2016, 2016 to 2019, and 2019 to 2022 were calculated and mapped (Table 4.3). The results 2013-2016 revealed that 451.47km^2, 632.58km^2, 4498.51km^2, 17578.65km^2, and 80.90 km^2 of water bodies, urban lands, barren lands, vegetation cover, and palm grove and forest areas, respectively, were unchanged. The maximum extent was stable in farming lands (17578.65 km^2), followed by barren lands (4498.51 km^2). The highest conversion occurred in vegetation lands to bare lands (6313.74 km^2) and (811.42 km^2) to urban lands during the same period. The maximum change of the bare lands and palms into urban lands was 134.50 and 1.98 km^2, respectively.

Table 4.3 Land use and land cover change matrix area (km^2) for the water years 2013–2016, 2016–2019, 2019–2022, and 2013–2022, for the Diyala River Basin.

		2016					
	Class	WB	UL	BL	VL	PL	Total
2013	WB	**451.5**	15.5	15.7	17.4	0.03	500.1
	UL	45.0	**632.6**	333.7	252.7	3.8	1267.8
	BL	40.3	134.5	**4498.5**	1085.8	0.3	5759.3
	VL	549.3	811.4	6313.7	**17578.6**	62.3	25315.3
	PL	0.2	1.9	2.3	45.6	**80.9**	131.0
	Total	1086.1	1595.9	11163.9	18980.1	147.2	**32973.5**
		2019					
	Class	WB	UL	BL	VL	PL	Total
2016	WB	**546.5**	44.5	33.7	34.4	2.02	661.1
	UL	69.9	**757.6**	484.8	277.7	15.8	1605.8
	BL	171.2	241.5	**7510.5**	1591.9	15.3	9530.3
	VL	181.3	490.4	4939.7	**15370.1**	42.3	21023.7
	PL	0.2	4.9	3.3	47.6	**95.4**	151.5
	Total	969.1	1538.9	12972.0	17321.6	170.7	**32972.5**
		2022					
	Class	WB	UL	BL	VL	PL	Total
2019	WB	**203.8**	101.8	207.9	145.00	4.46	663.07
	UL	5.9	**962.8**	353.86	275.37	8.83	1606.83
	BL	41.2	331.0	**6890.38**	2272.99	26.27	9561.80
	VL	11.7	212.9	1039.48	**19726.33**	32.83	21023.28
	PL	0.06	1.4	3.01	33.01	**80.08**	117.54
	Total	262.7	1609.9	8494.72	22452.70	152.47	**32972.51**
		2022					
	Class	WB	UL	BL	VL	PL	Total
2013	WB	**190.1**	78.9	98.6	129.9	2.4	500.0
	UL	5.4	**752.4**	368.4	136.5	6.4	1269.2
	BL	4.7	206.0	**5098.6**	446.3	2. 9	5758.4
	VL	24.7	580.1	2923.2	**21713.8**	73.6	25315.4
	PL	0.25	23.9	21.9	26.3	**57.0**	129.5
	Total	225.2	1641.4	8510.8	22452.8	142.3	**32972.5**

The modification identification matrix was computed using the pixel-by-pixel approach from 2016 to 2019 as shown in (Table 4.3). The results displayed that vegetation lands have been decreasing during this period and altering into bare lands, urban lands, or new types. The stable areas, according to calculations,

covered 15370.05 km^2, and the largest area conversion discovered in the arid plains, 4939.74 km^2. The palm area's transition trend showed that 95.40 km^2 is unchanged. A large part of the palm industry was transformed into vegetation and urban. It is interesting to note that urban occurred mainly in the lower part of DRB areas because people prefer to reside in the lowlands as living costs are low compared to mountain lands and along the roadways.

The change detection results from 2019 to 2022 showed that 19726.33 km^2 of VL were unaffected, but 1039.48, 212.97, 32.83, and 11.67 km^2 of areas were converted into BL, UL, PL, and WB, respectively. The maximum advance of the BL class by UL extents was 331 km^2. For WB, UL, BL, and PL, about 203.83, 962.82, 6890.38, and 80.08 km^2 areas were stable. Furthermore, from 2013 to 2016, 2016 to 2019, and 2019 to 2022, it has been found that more land was transformed into bare lands (6313.74, 4939.74, and 1039.48 km^2) and urban (811.42, 490.42, and 212.97 km^2) from vegetation lands.

The overall LU and LC conversion between 2013 and 2022 showed that the areas of built-up (580.13 km^2) and barren (2923.18 km^2) expanded the common terrestrial vegetation cover more than the two previous transitional times. In contrast to the previous two transition matrices, the conversion of barren indicated that all classes except from this gained the regions. Because urban areas encroached more quickly than the others, the highest conversion was seen in arid regions. The barren class encroached on 2923.18 km^2 of vegetation area within nine years, which was the longest time period of all categories.

4.4.1 Results of NDVI and LST

From 2013 to 2022, the minimum values of NDVI ranged from -0.25 to -0.29, the maximum values of NDVI ranged from 0.61 to 0.65, and the average shows the same statistics (Figure 4.3 and Table 4.4). The total basin area has witnessed a decline in plant cover; in 2013 and 2016, the maximum NDVI value was 0.61, which shows that vegetation covers, such as grassland and forest areas, were

expanded, while the minimum NDVI values were -0.25 to -0.28, in that order, which reveals that DRB has a sufficient amount of water bodies. Between 2019 and 2022, the maximum NDVI values were 0.67 and 0.65, which shows that vegetation cover is expanding, and the minimum NDVI values were -0.26 to -0.29, in that order, which implies enough water bodies and bare soil (Table 4.4).

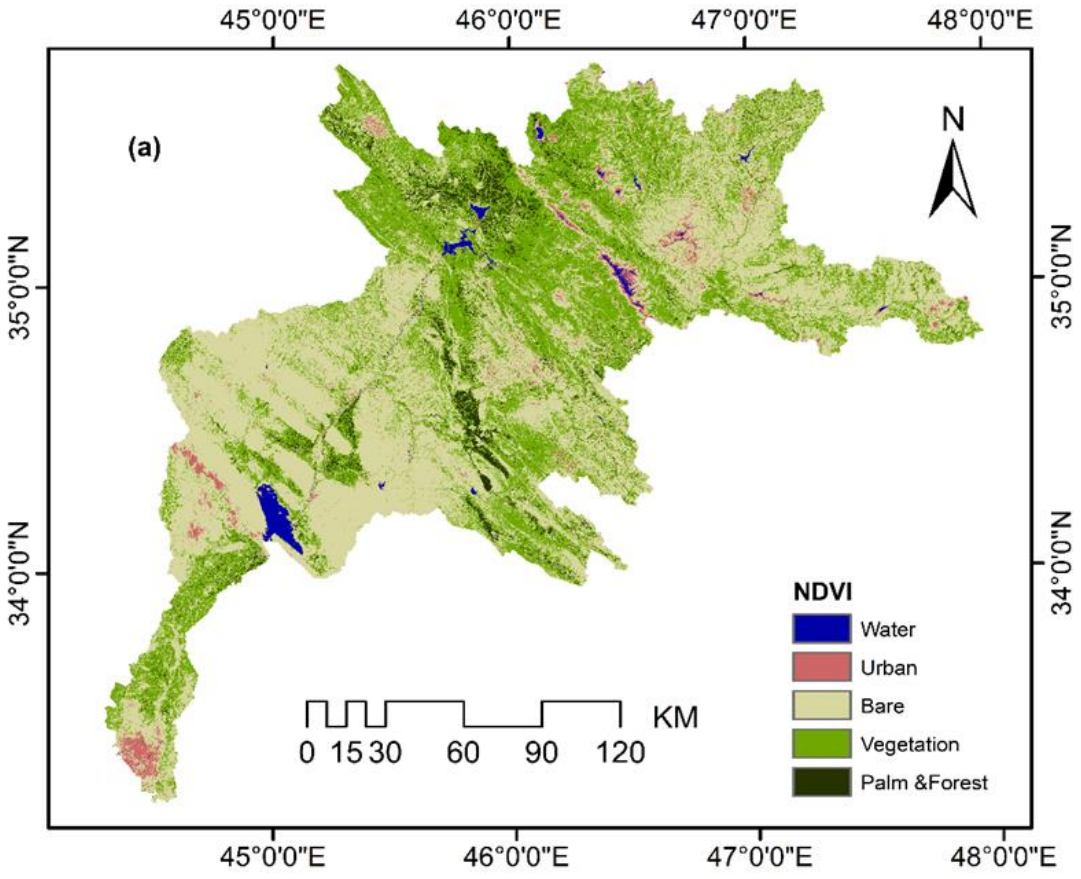

(a):Spatiotemporal alteration based on NDVI at 2013.

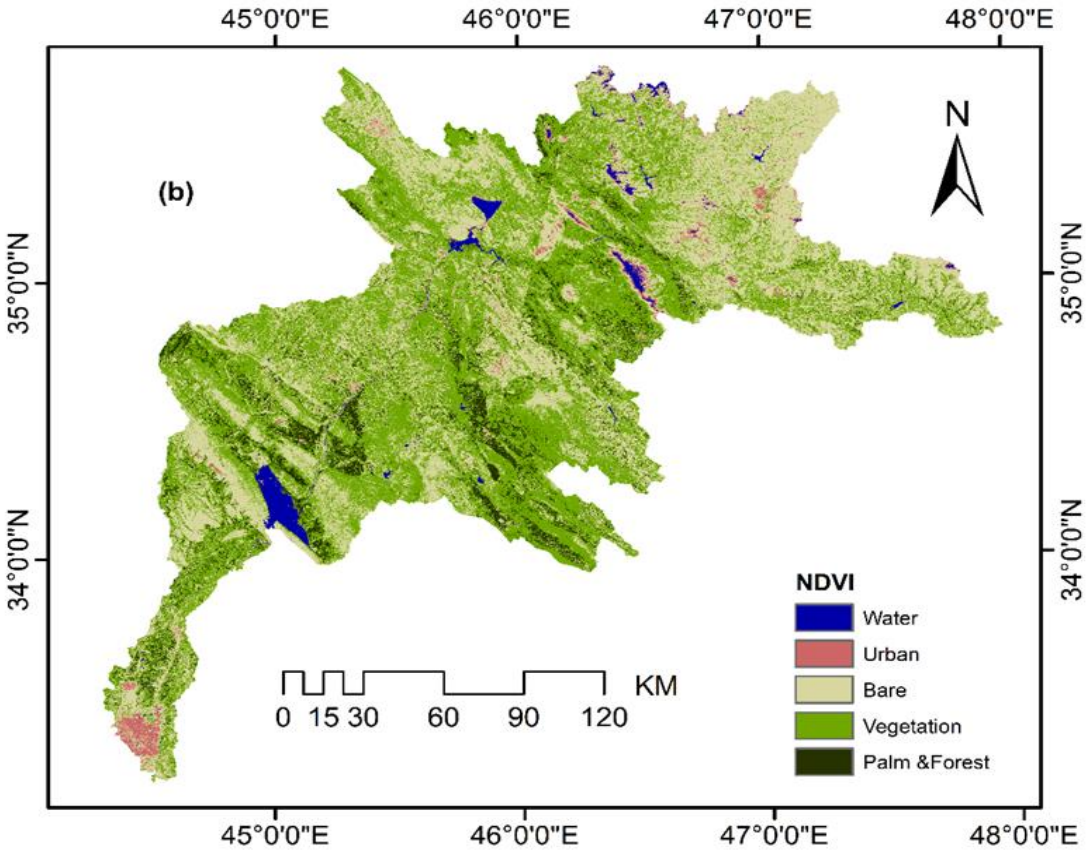

(b):Spatiotemporal alteration based on NDVI at 2016.

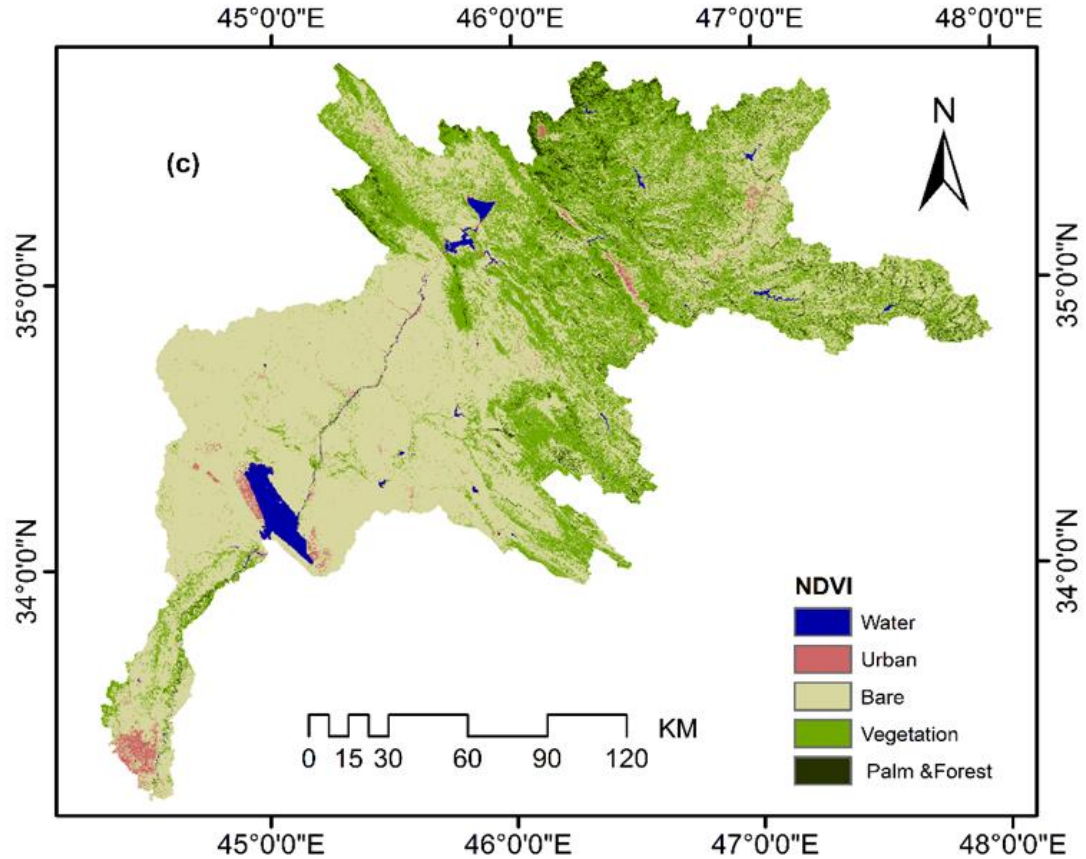

(c):Spatiotemporal alteration based on NDVI at 2019.

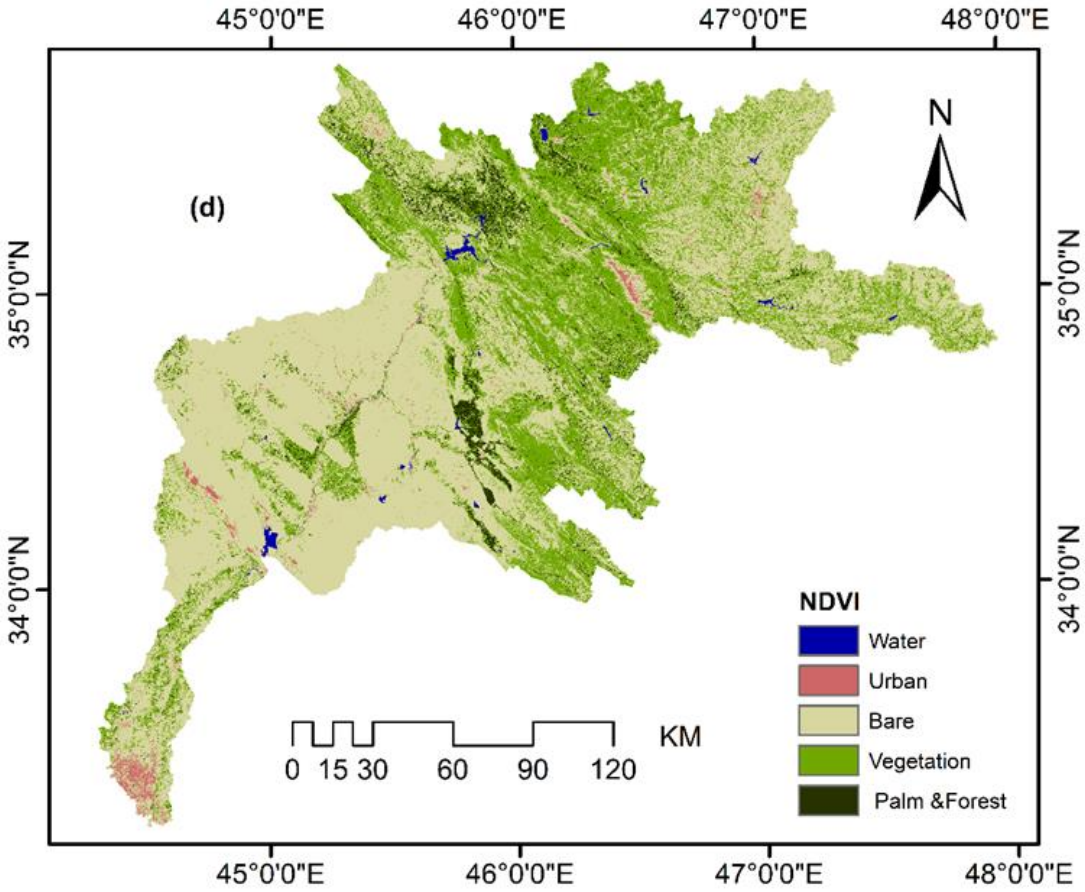

(d):Spatiotemporal alteration based on NDVI at 2022.

Figure 4.3 The Normalized Difference Vegetation Index (NDVI) in the Diyala Basin River over the study period.

Table 4.4 Descriptive statistics for weather parameters and Normalized Difference Vegetation Index (NDVI) values for the period 2013, 2016, 2019, and 2022 for the Diyala River Basin.

Year	NDVI				Weather Variables								LST	
					Temperature (C)				Precipitation (mm)					
	Min[1]	Max[2]	Me.[3]	SD[4]	Min[1]	Max[2]	Me[3]	SD[4]	Min[1]	Max[2]	Me[3]	SD[4]	Max[2]	Min[1]
2013	-0.25	0.61	0.18	6.4	5.1	31	18.05	5	275.33	378.26	326.8	30.2	47.2	-10.2
2016	-0.28	0.61	0.17	5.7	1.3	31.2	16.25	5.36	369.83	593.76	481.8	70.3	43.4	-11.5
2019	-0.26	0.67	0.21	7.2	9.7	34.9	22.3	5.31	432.06	603.54	517.8	56.72	47.2	1.7
2022	-0.29	0.65	0.18	6.3	4.6	33.8	19.2	5.18	132.3	369.12	250.7	93.17	49.2	-1.2

[1]Minimum; [2]Maximum; [3]Mean; [4]Standared deviation

The value of NDVI shows decline in vegetation cover, mainly in the lower portion of the basin extent (Figure 4.3 and Table 4.5). The upper part of the basin consists of topography with grasslands and trees. However, the NDVI-based vegetation

mass is less in the interior portion of the study area and less in the lower part of the basin (Figure 4.3). A smaller amount of precipitation and high air temperatures are observed in the lower part of the basin (Figures 4.3a and 4.3b). These results are consistent with the research performed by (Gaznayee 2021; Gaznayee et al., 2022), and both studies concluded rises in the severity and occurrence of drought over the basin. An increase in LST, a decline in plant cover, and a shortage of average rainfall were the main properties of the studied basin. Climate conditions have reduced the vegetated cover, and topographical inconsistency is another factor that has affected vegetation cover.

Table 4.5 The area coverage and percentage of the entire area for the Diyala River Basin in the years 2013, 2016, 2019, and 2022 for the Normalized Difference Vegetation Index.

	Area							
	2013		2016		2019		2022	
LU/LC*	Km^2	%	Km^2	%	Km^2	%	Km^2	%
WB	353.4	1.1	560.2	1.7	550.0	1. 7	165.9	0.5
UL	784.8	2.4	695.5	2.1	529.2	1.6	455.1	1.4
BL	18433.8	55.9	13222.5	40.1	20252.1	61.4	20374.2	61.8
VL	12001.4	36.4	16128.7	48.9	10547.8	31.9	10515.2	31.9
PL	1402.3	4.3	2368.7	7.2	1096.5	3.3	1465.2	4.4

Linear regression analysis was utilised to discover correlations between LST and NDVI, and the results show that LST and NDVI were adversely correlated by regression analysis as shown in (Figure 4.4).

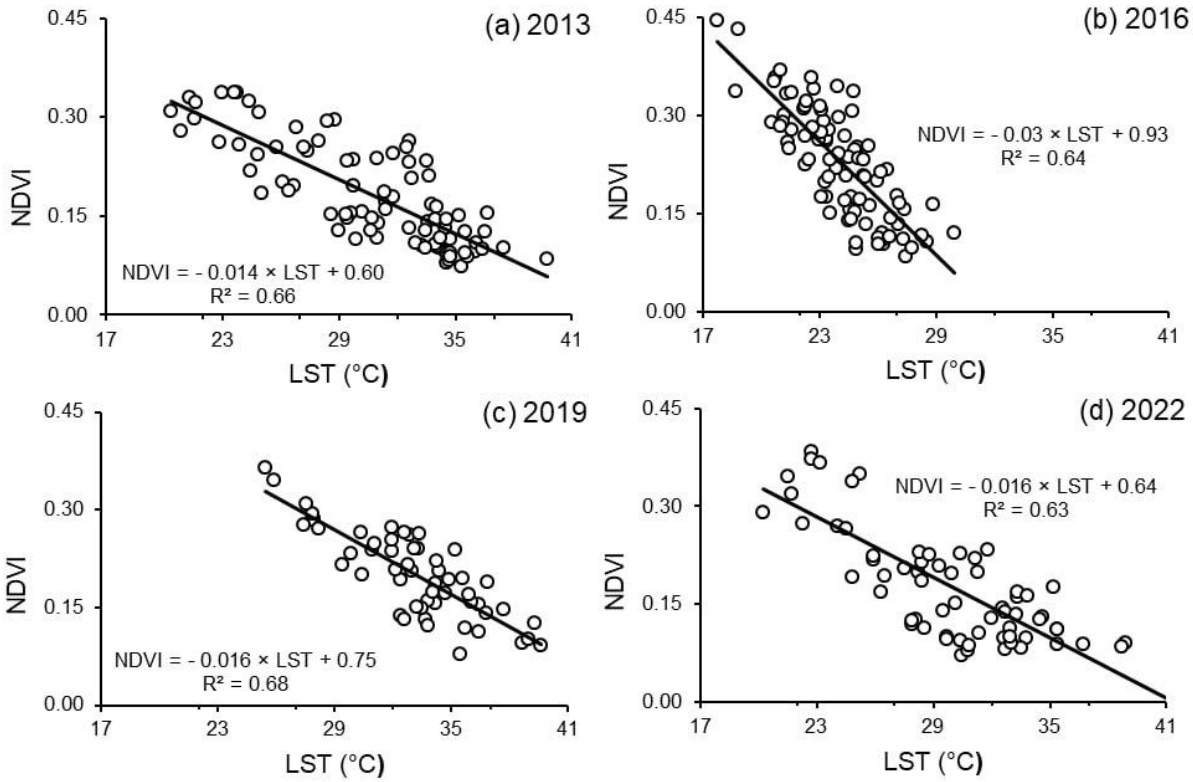

Figure 4.4 Alteration maps of the Normalized Difference Vegetation Index (NDVI) and Land Surface Temperature (LST) of the Diyala Basin in (a) 2013; (b) 2016; (c) 2019; and (d) 2022.

4.4.2 Result of climate factors and NDVI

Climate data are collected from the National Aeronautics and Space Administration (NASA). The data were then correlated with ground-based values and visualised using the Arc GIS 10.8 programme. The spatial distribution maps of the long-term mean air temperature and precipitation are shown in Figures 4.5a and 4.5b. When compared to Khanaqin, the long-term precipitation values changed from (300-360) mm at Baghdad station to (460-470) mm. A notable difference between the upper and lower sub-basins was the amount of precipitation (Figure 4.5a). The mean air temperature of the basin ranged from 10.8513.15 °C, 13.1515.81 °C, 15.8218.48 °C, and 18.4921.24 °C at the upper and middle parts of the basin to more than 24.17 °C at the upper part of the basin (Figure 4.5b).

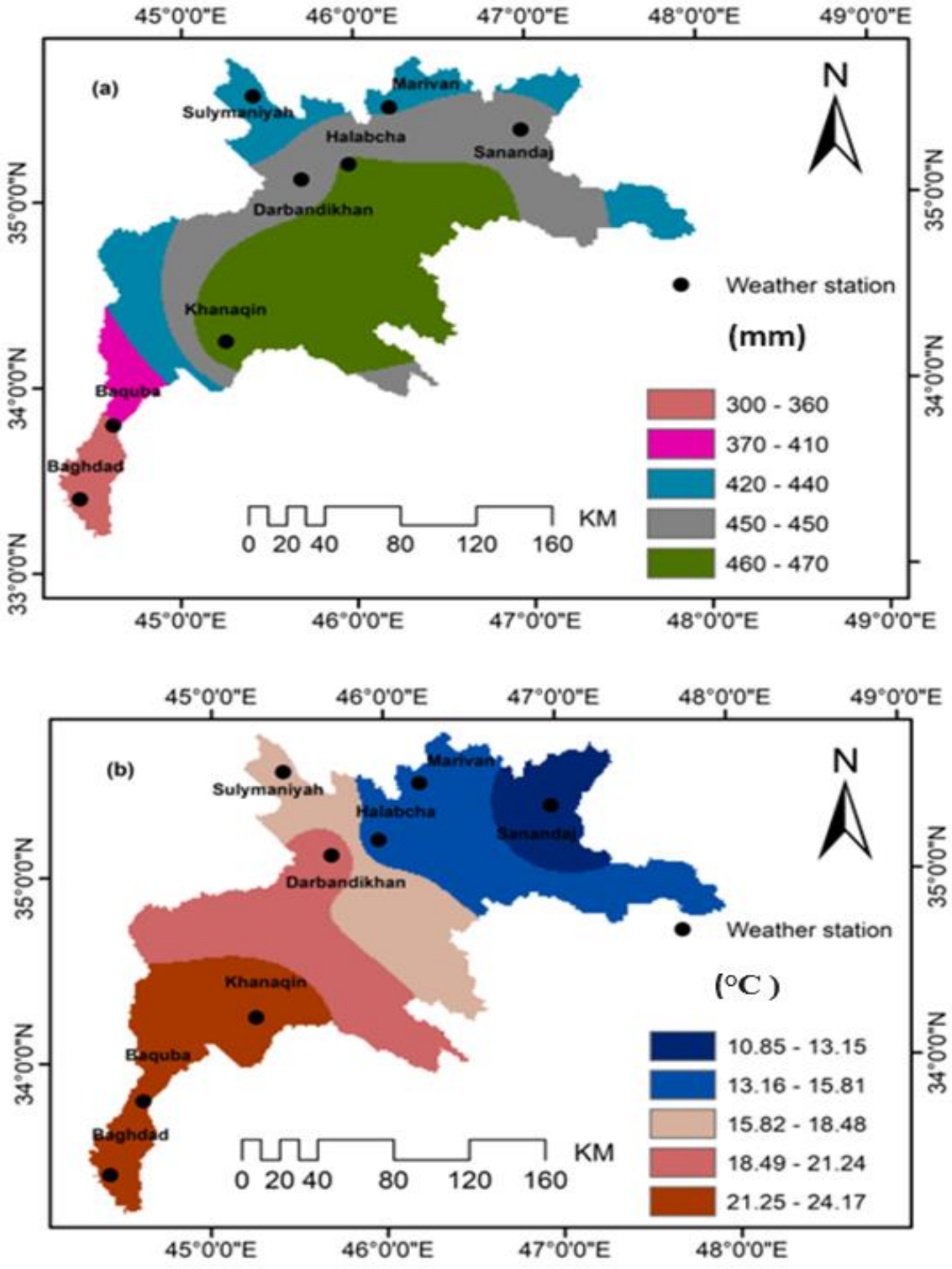

Figure 4.5 The spatial distribution of the (a) average precipitation and (b) mean air temperature, of the Diyala Basin. (monthly average).

To determine the relations between meteorological variables and NDVI, regression analysis (R^2) for the annual reference period for rainfall, temperature, and NDVI has been implemented (Figure 4.6). Precipitation and mean air temperature were progressively linked with LU/LC among different environmental factors. The trend of the regression coefficient R^2 indicates that there is a negative association between temperature and NDVI. Regression coefficients (R^2) of 0.5, 0.67, 0.63, and 0.63 were detected for 2013, 2016, 2019, and 2022, respectively. However, precipitation has a positive correlation with NDVI throughout the same period of 0.5, 0.67, 0.4, and 0.5, respectively. The analysis reveals that NDVI essentially declines in areas where temperatures increase and precipitation decreases. Interestingly, the temperature in urban areas was greater than the temperature in plant-covered areas. Valuation and assessment of the built-up location need figures and an understanding of LST.

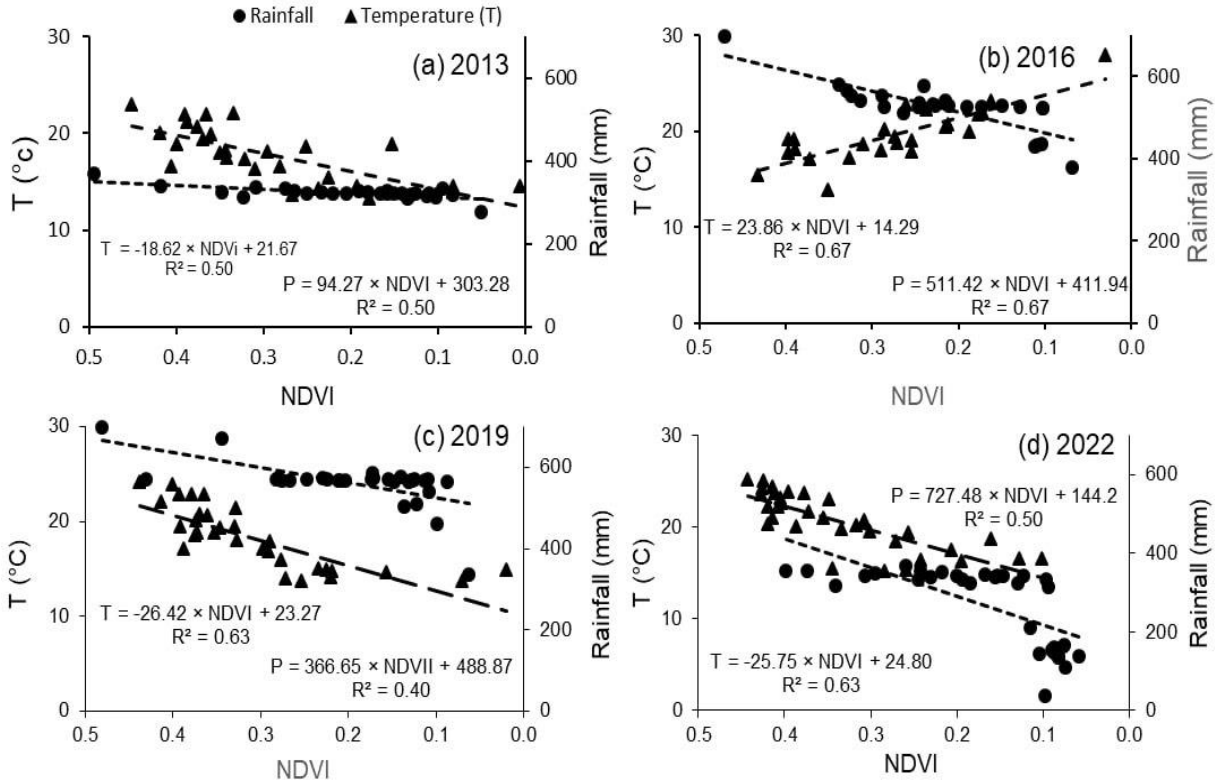

Figure 4.6 Correlations among Mean air temperature (T) and precipitation (P) and the Normalized Difference Vegetation Index (NDVI) of the Diyala Basin in (a) 2013; (b) 2016; (c) 2019; and (d) 2022.

In evaluating the growth in agricultural lands brought on by the development of environmental protection laws and the prevention of recording over the past few years, the development of living standards, increased awareness among residents of these parts, and ongoing synthetic afforestation in that zone, the territory, shrub area, and trees may be crucial factors (Mustafa, 2015; Gaznayee et al., 2022). The variations of agricultural drought in terms of NDVI were observed as LST variations. LST and NDVI relations exhibit bad connections in the research basin, according to Figure 4.4, which looks at the generalizability of the represented LST and NDVI correlations about weather drought observation and valuation. NDVI and LST often have a negative association since NDVI values rise as LST values fall. The associations between LST and NDVI are often negative (Sun et al., 2010; Gaznayee et al., 2022). Except for a negligible rise at some sites, there were maximum changes in NDVI in the northeast and southeast, where rainfall was higher than before in some parts. NDVI variations were seen throughout the study period, and the index saw a significant rise in 2019 and 2022.

The NDVI index regularly increased with the increase in precipitation and decrease in temperature in the upper parts of DRB, which has resulted in a growing trend in the vegetation of the northeast as shown in (figure 4.3, figure 4.5). Conversely, constant LST increases and declining precipitation caused continuous decreases in the vegetation covering the lower part of the basin. The drought in semi-arid regions considerably leads to ecological degradation as it limits vegetation cover growth and exposes the soil to loss (Gaznayee et al., 2022). The spatiotemporal variability of LST-NDVI correlation on universal scales has been considered by several researchers (Julien and Sobrino, 2010) and was founded on the hypothesis that complementary statistics in these researches would deliver an extra vigorous description for many occurrences at the ground's surface. This study's NDVI varies owing to spatiotemporal rainfall variability (Goward et al., 2002). Accordingly, NDVI is a reasonably worthy sign of

precipitation deficiency in the region, and warmer temperatures are effective for plants growth (Mahdi and Mohammed 2022). The use of the NDVI-LST-based indices regression formula must be restricted to local times and places where harmful associations are seen, rather than on a global scale. The application of the NDVI-LST-based indices regression formula must be limited to local areas and times wherever deleterious relationships are observed and not on an international level. Depending on whether energy temperature (a positive slope) or water (a negative slope) serves as growth constraints for the vegetation, the LST-NDVI slope sign may be affected. The latter can occur at lower latitudes, especially in dry terrain, whereas the former is more common at high latitudes or in tropical evergreen forests (Gaznayee et al.2022;Mahdi and Mohammed2022).

4.4.3 Change in Normalized Difference Vegetation Index

The most drought-prone periods, as determined by vegetation growth, were the years 2017–2021 and 2022, according to the findings in Table 4.6 and Figure 4.7. The vegetation cover was noticeably lower in these years compared to other years. The extent of the drought peaked in 2021, when it reduced the vegetative cover to 6816.81 km2, or 20.67% of the entire study area. The vegetation coverage in 2021 deviated (-28.48%) from the average, which is 38.45% on average over the 2013–2022 period. From 2013 to 2022, the Diyala Basin's NDVI spatiotemporal distribution is shown in Figure 4.7 and Table 4.6.

Table 4.6 Descriptive statistics NDVI and vegetation cover characteristics for the study area over the study area

Year	NDVI				Area (km^2)	Coverage %	Fluctuation %
	Max	Min	Mean	SD			
2013	0.61	-0.25	0.18	0.61	13403.71	40.65	-8.5
2014	0.63	-0.28	0.175	0.64	12967.08	39.32	-9.83
2015	0.65	-0.37	0.14	0.72	14451.85	43.83	-5.32
2016	0.61	-0.28	0.165	0.63	18497.41	56.09	6.94
2017	0.67	-0.3	0.185	0.69	11865.02	35.98	-13.17
2018	0.62	-0.3	0.16	0.65	13284.99	40.29	-8.86
2019	0.67	-0.26	0.205	0.66	11644.31	35.31	-13.84
2020	0.64	-0.31	0.165	0.67	12324.34	37.37	-11.78

Table 4.6: Continued

2021	0.63	-0.37	0.13	0.71	6816.811	20.67	-28.48
2022	0.65	-0.25	0.2	0.64	11980.41	36.33	-12.82

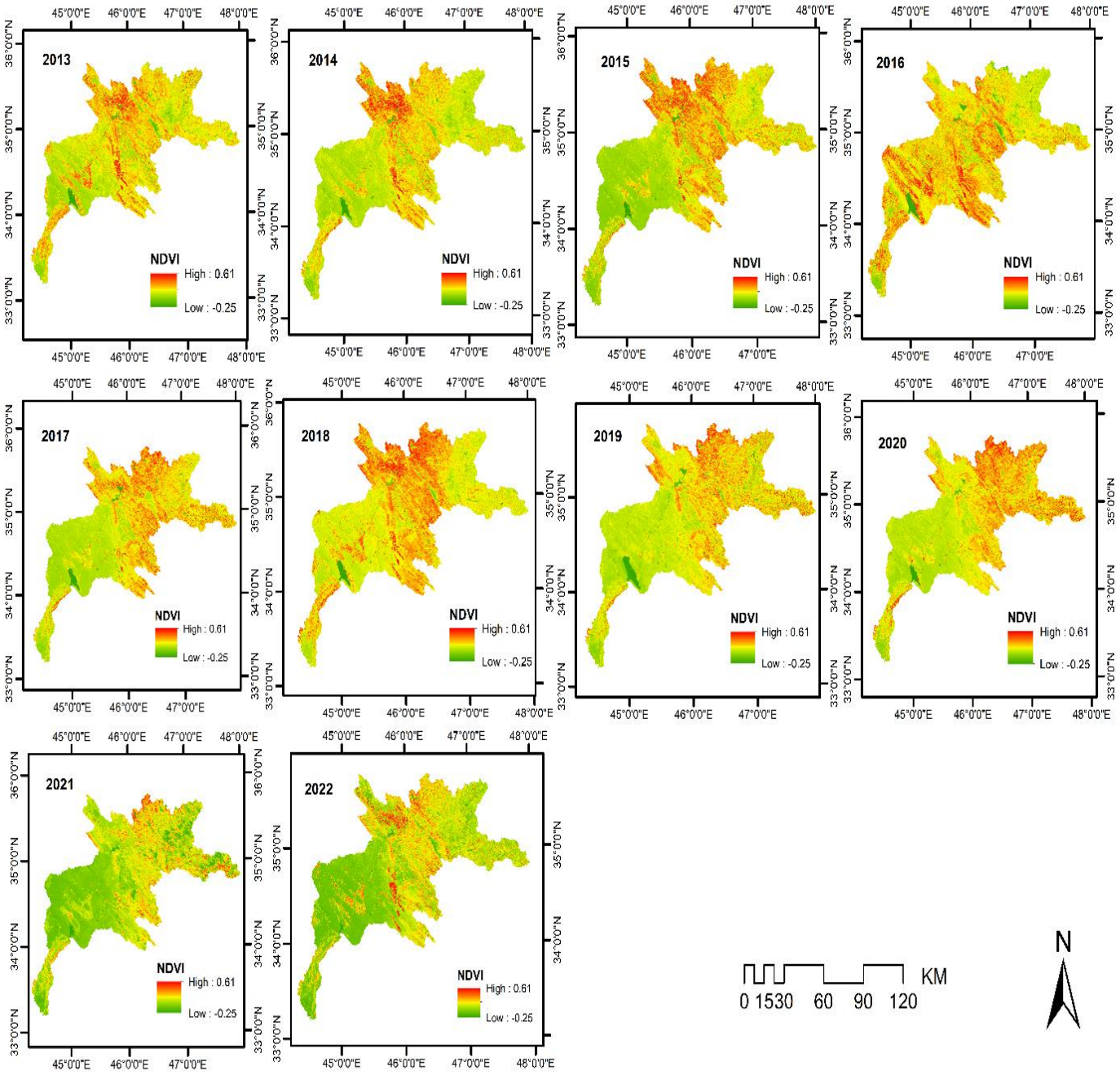

Figure 4.7 Variations in the study area's Normalized Difference Vegetation Index (NDVI-based) vegetation cover Variations in the study area's NDVI-based vegetation cover over time from 2013 to 2023.

4.5.1 Vegetation Condition based on Vegetation Cover Index

According to the VCI findings, severe droughts occurred in 2013, 2016, and 2022. Less than or equal to 10 (severe drought) and more than 40 were among the VCI results (no droughts). Table 4.7 shows that the most critical years for drought events were 2013, 2019, and 2022, although the vegetation cover was extraordinarily decreased compared to the 2016 year over the examined period. The droughts peaked in 2022, their highest severity; consequently, 2022 is considered the driest in the research period. Based on the geographical patterns of drought severity in the DRB, the results indicated that the whole research region experienced mild to severe drought during the study period, particularly in 2013 and 2022. Except for many minor northern locations, 2022 was an extremely poor drought year with harsh conditions throughout the region. The severe and extreme drought parts in the north, eastern, middle, and southern areas of the studied region were 5727.1 km2 (47.8%), 644.3 km^2 (5.4%), 635.3 km^2 (5.3%), and 653.2 km^2 (5.5%), for extreme, severe, moderate, mild, and no drought, respectively. In general, the VCI, Table 4.7, and Figure 4.8 show that the southern and middle zones of the DRB are the most affected by extreme droughts.

Table 4.7 Areas and rate of the Drought Severity Categories based on Vegetation Condition Index (VCI) values for the period 2013, 2016, 2019, and 2022 for the Diyala River Basin.

Year			2013	2016	2019	2022
Areas and rate of the Drought Severity Categories	Extreme VCI ≤ 10	(km^2)	3551.1	3837.2	3188.8	5727.1
		(%)	26.5	20.7	27.4	47.8
	Severe 10 < VCI ≤ 20	(km^2)	1283.3	676.4	1078.7	644.3
		(%)	9.6	3.6	9.3	5.4
	Moderate 20 < VCI ≤ 30	(km^2)	1391.2	658.5	1224.2	635.3
		(%)	10.4	3.6	10.5	5.3
	Mild 30< VCI ≤ 40	(km^2)	1151.8	647.9	993.2	653.2
		(%)	8.6	3.5	8.5	5.5
	No Drought VCI > 40	(km^2)	6026.3	12677.4	5159.5	4320.4
		(%)	44.9	68.5	44.3	36.1

Table 4.7: Continued

Total Vegetation cover	(km^2)	13403.7	18497.4	11644.3	11980.4
	(%)	100	100	100	100

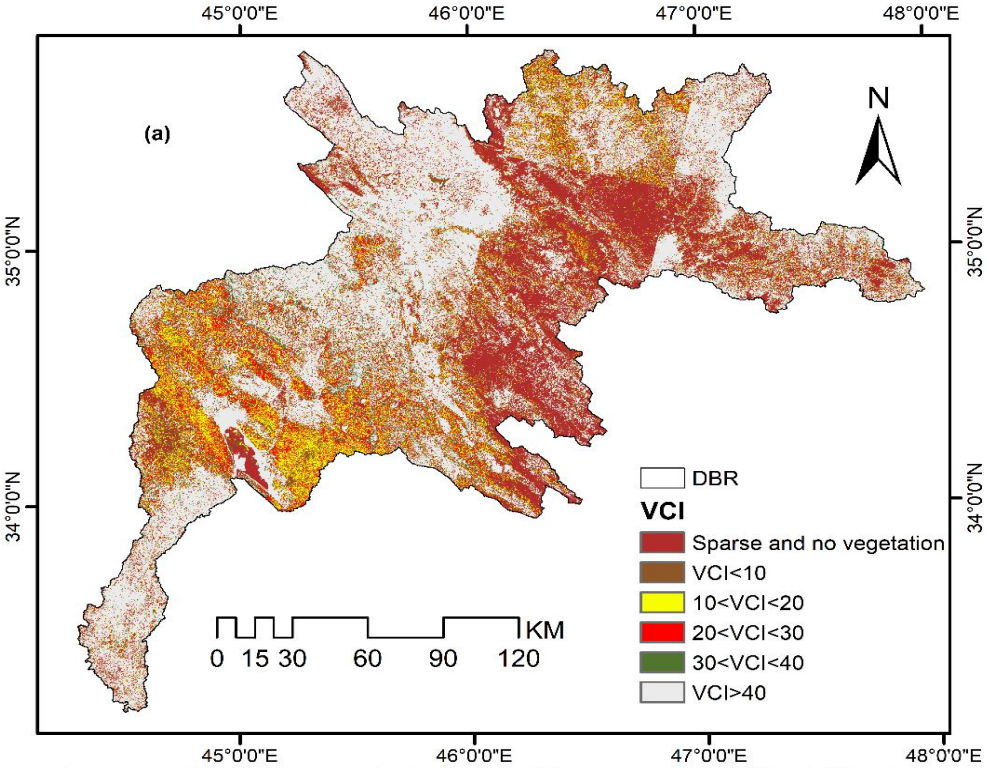

(a) :variations of vegetation condition index (VCI) of 2013

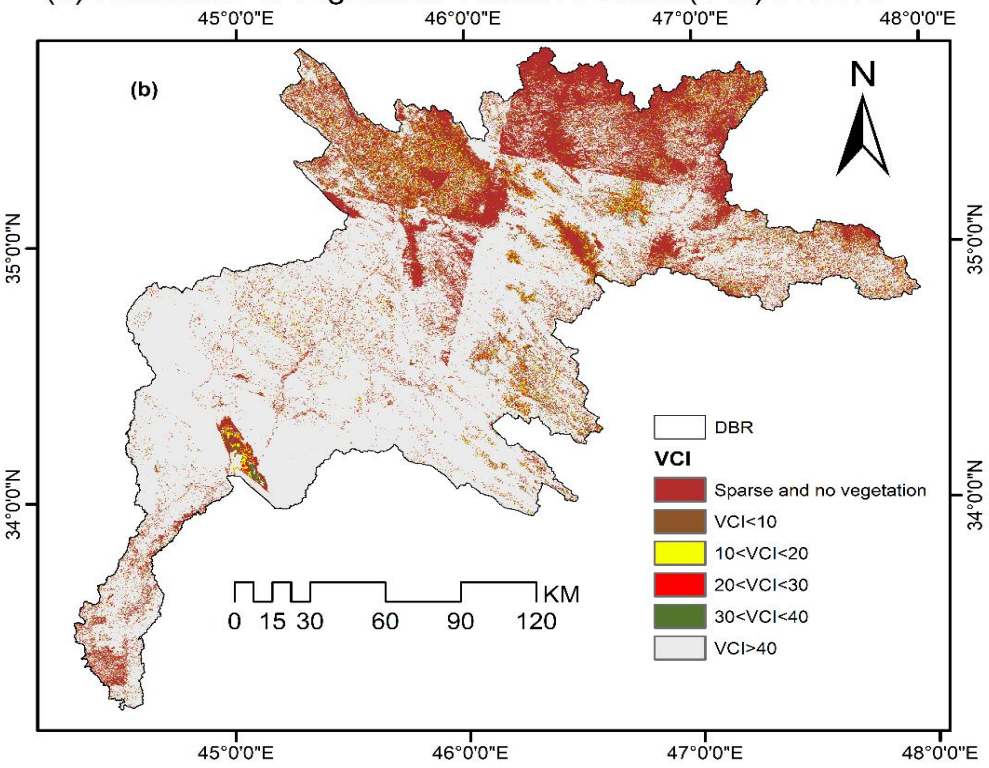

(b) :variations of vegetation condition index (VCI) of 2016

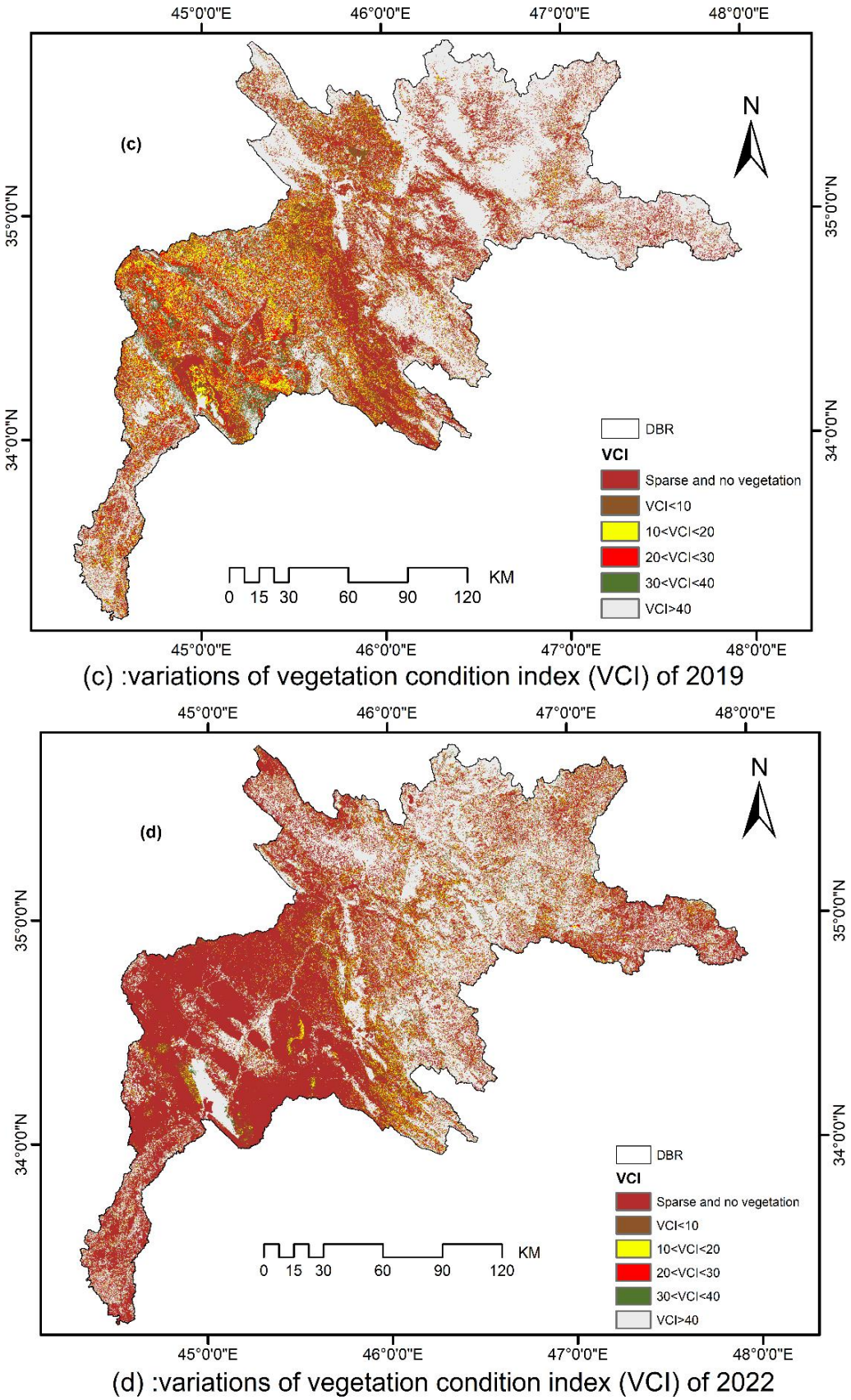

Figure 4.8 Spatiotemporal variations in Diyala Basin River over the study period.

4.5.2 Change in Vegetation Cover Index (VCI)

The VCI results showed that there had been severe drought events in 2017, 2021, and 2022. According to the VCI index, which has values ranging from 0 for non-vegetative to 100 for dense vegetation, the most critical years for drought were 2017, 2021, and 2022, while vegetation cover was noticeably decreased in comparison to the other years throughout the investigated period. Because 2021 was the year when the drought was at its worst, during the time of the study, it was the driest year. Taking into account the spatial patterns of the Diyala catchment's drought severity, the results showed that mild to severe drought affected the entire study area between 2013 and 2022, especially in 2021 and 2022. With the exception of a few small northern patches, Diyala experienced a terrible drought in 2021. In the northern, central, eastern, southeastern, and southern parts of Diyala, the combined areas of severe and extreme drought were 3704.34 km^2 (54.34%), 800.54 km^2 (11.74%), 532.59 km^2 (7.81%), and 404.70 km^2 (5.94%), respectively. The south and middle regions of Diyala typically suffer the most from severe droughts, according to the VCI (Table 4.8 and Figure 4.9a, 4.9b). Additionally, the results showed that Diyala experienced a very severe drought in 2022, with 3530.14 km^2 (29.47%), 1192.53 km^2 (9.95%), 1150.47 km^2 (9.6%), and 1202.42 km^2 (10.04%), respectively, for the categories of extreme, severe, moderate, mild, and no drought. The largest class area was found in 2017, with a protracted extreme drought area of 3319.94 km^2 (27.98%), according to the results of the second-highest geographical region for Extreme Drought Class (VCI = 10).

Table 4.8 Drought Severity Category areas and rates for the Diyala River basin from 2013 to 2022, based on Vegetation Condition Index (VCI) values.

Year	Class 1[a]		Class 2[b]		Class 3[c]		Class 4[d]		Class 5[e]		TVC[f]
	Area		Area		Area		Area		Area		Area
	km^2	%	km^2	%	km^2	%	km^2	%	km^2	%	km^2
2013	1909.2	14.2	1388.2	10.4	1651.9	12.3	1587.6	12.8	6866.91	51.2	13403.7
2014	1333.8	10.3	1330.0	10.3	1976.6	15.2	1792.3	13.8	6534.3	50.4	12967.1
2015	2758.9	19.1	1509.5	10.4	998.9	6.9	888	6.1	8296.7	57.4	14451.9
2016	1998.1	10.8	1029.5	5.6	1227	6.6	1271.9	6.9	12970.9	70.1	18497.4
2017	3319.9	28	1633.3	13.8	1083.1	9.1	920.5	7.8	4908.2	41.4	11865.0
2018	1910.0	14.4	1178.7	8.9	1788.6	13.5	1552.9	11.7	6854.7	51.6	13285
2019	1149.6	9.9	1430.5	12.3	1836.1	15.8	1627.7	14	5600.35	48.1	11644.3
2020	2394.6	19.4	2310.2	18.7	1523.9	12.4	882.5	7.2	5213.13	42.3	12324.3
2021	3704.3	54.3	800.5	11.7	532.6	7.8	404.7	5.9	1374.64	20.2	6816.8
2022	3530.1	29.5	1192.5	10	1150.5	9.6	1202.4	10.0	4904.85	40.9	11980.4

[a]VCI values ≤ 10 (extreme); [b] $10 <$ VCI values ≤ 20 (severe); [c]$20 <$ VCI values ≤ 30 (moderate); [d]$30 <$ VCI values ≤ 40 (mild); [e]VCI values > 40 (no); [f]Total Vegetation Cover Area.

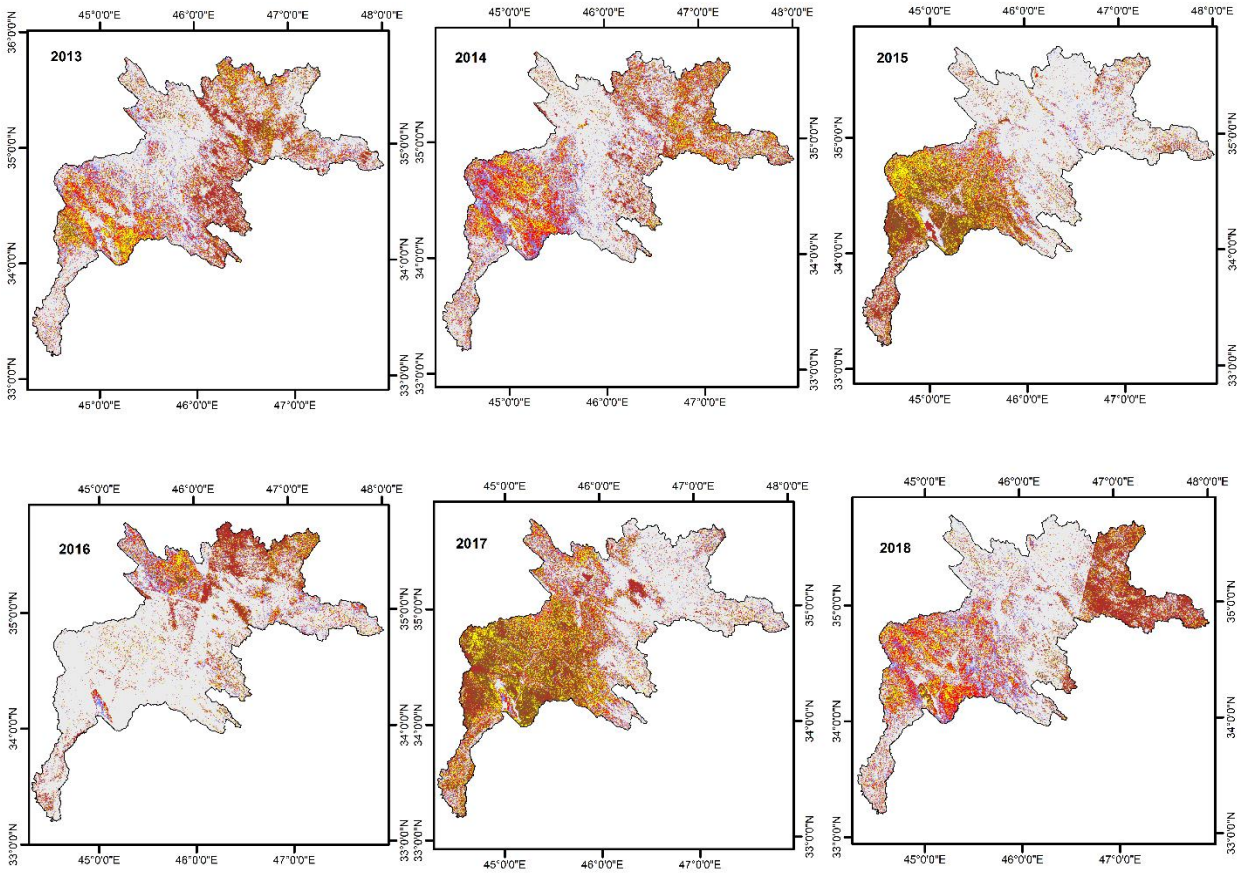

Fig. (4.9a): Classification of draught severity based on VCI for period from 2013 to 2018 in the Diyala River Basin.

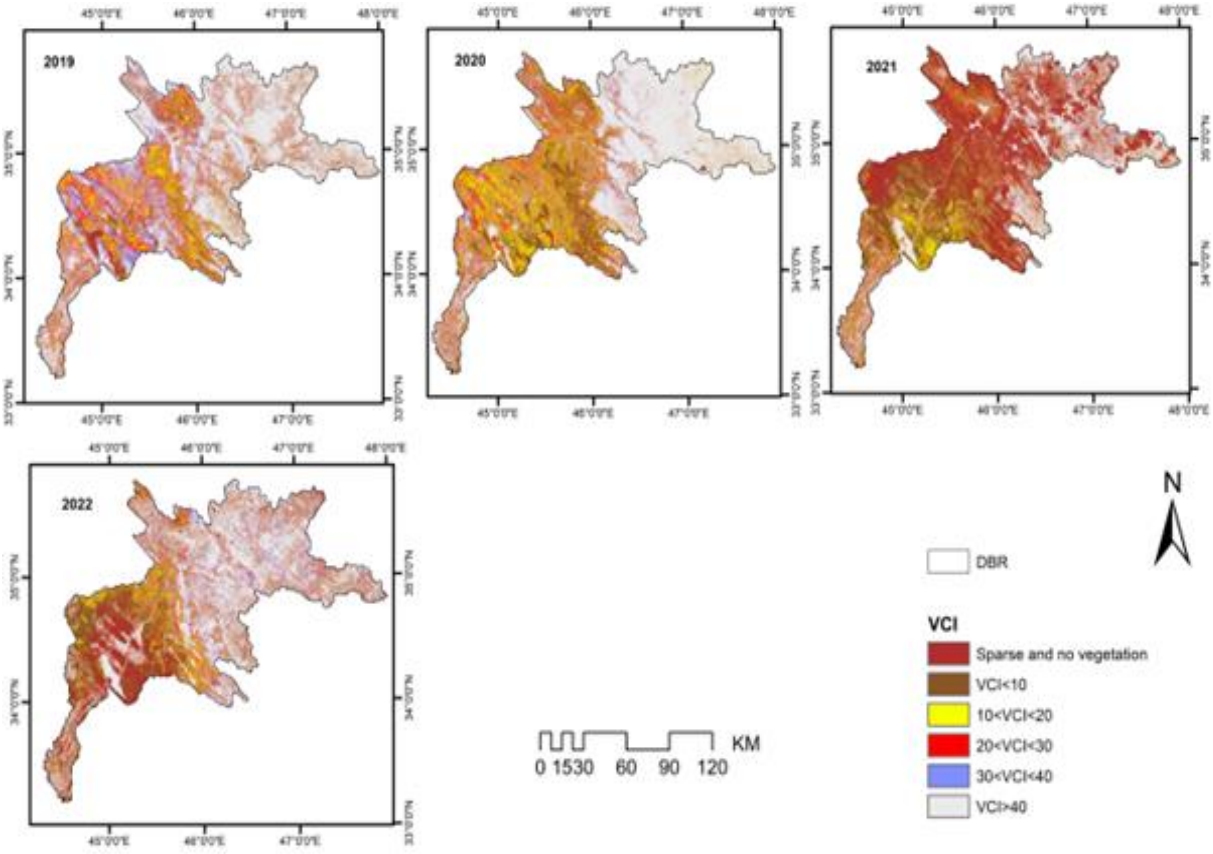

Fig. (4.9b): Classification of draught severity based on VCI for period from 2019 to 2022 in the Diyala River Basin.

4.6.1 Area changes of Derbendikan Lake by NDWI

Combining the NDWI and VCI to monitor the Derbendikan Lake (DLK) water surface area and river water levels is a very efficient way to investigate drought patterns. According to NDWI values, the water surface area of the DLK experienced a particularly severe drought effect in 2021 and 2022 (Table 4.9, Figure 4.10). Higher VCI values, a smaller DLK surface area, and lower average precipitation were the defining characteristics of the years discussed. Over the ten years under study, the DLK's surface area changed (Table 4.9, Figure 4.10). The surface area's highest and lowest values were 109.06 and 119.66 km2, respectively, in 2016 and 2019, while 44.63 and 52.61 km^2, respectively, were recorded in 2021 and 2022.

Table 4.9 The surface area of the Derbendikan Lake (DLK) and its percentage change from 2013 to 2022.

Water year	Area	Fluctuation[a]
	km^2	%
2013	63.13	3.4
2014	54.88	-4.85
2015	56.26	-3.47
2016	109.06	49.33
2017	107.80	48.07
2018	55.68	-4.05
2019	119.66	59.93
2020	82.40	22.67
2021	44.63	-15.1
2022	52.61	-7.12

[a]Fluctuation shows the variation around the average % of the DLK's surface area.

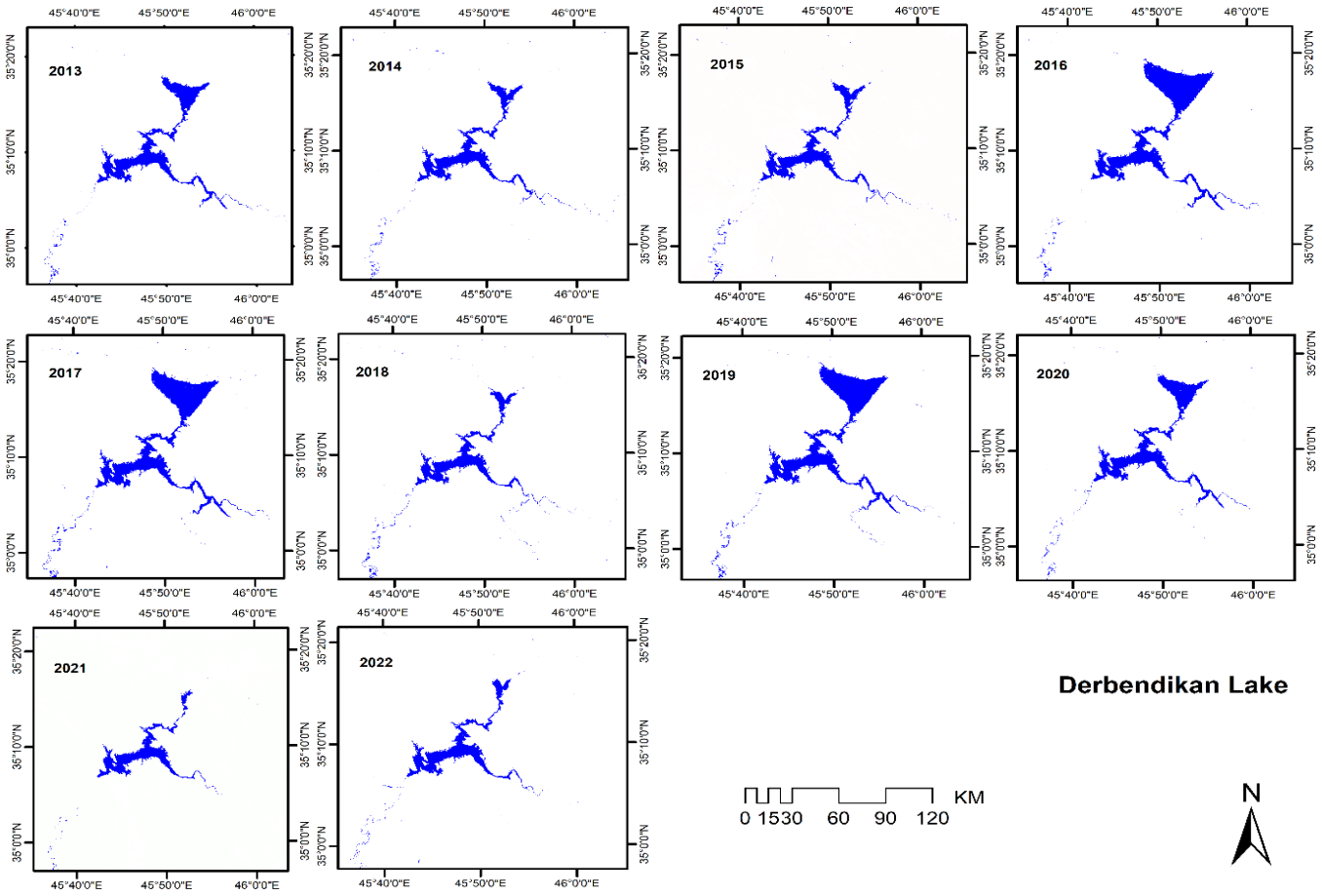

Figure 4.10 Derbendikan Lake (DLK) surface area variations in spatial distribution from 2013 to 2022.

4.6.2 Area changes in Hemrin Lake by NDWI

A very effective way to examine drought patterns is by using NDWI and VCI in conjunction to monitor the HLK's surface area and the river's water levels. Using the NDWI results, it was discovered that the drought's effects on the HLK's surface area were especially noticeable in 2021 and 2022. (Table 4.10, Figure 4.11). Lower VCI values, a smaller HLK surface area, and lower precipitation averages were all characteristics of the cited years. Over the ten years under study, the HLK's surface area changed (Table 4.10, Figure 4.11). Particularly, with surface areas of 317.03 and 360.86 km^2, respectively, the two years 2016 and 2019 had the largest surface areas. The two consecutive years 2021 and 2022 had small surface areas, measuring 66.79 and 31.84 km^2, respectively.

Table 4.10 The surface area of the Hemrin Lake (HL) and its percentage change from 2013 to 2022.

Water year	Area	Fluctuation[a]
	km^2	%
2013	181.87	6.7
2014	188.48	13.31
2015	123.31	-51.86
2016	317.03	141.86
2017	214.99	39.82
2018	237.51	62.34
2019	360.86	185.69
2020	187.45	12.28
2021	66.79	-108.38
2022	31.84	-143.33

[a]Fluctuation indicates the fluctuation around the average percentage of the surface area of the HL

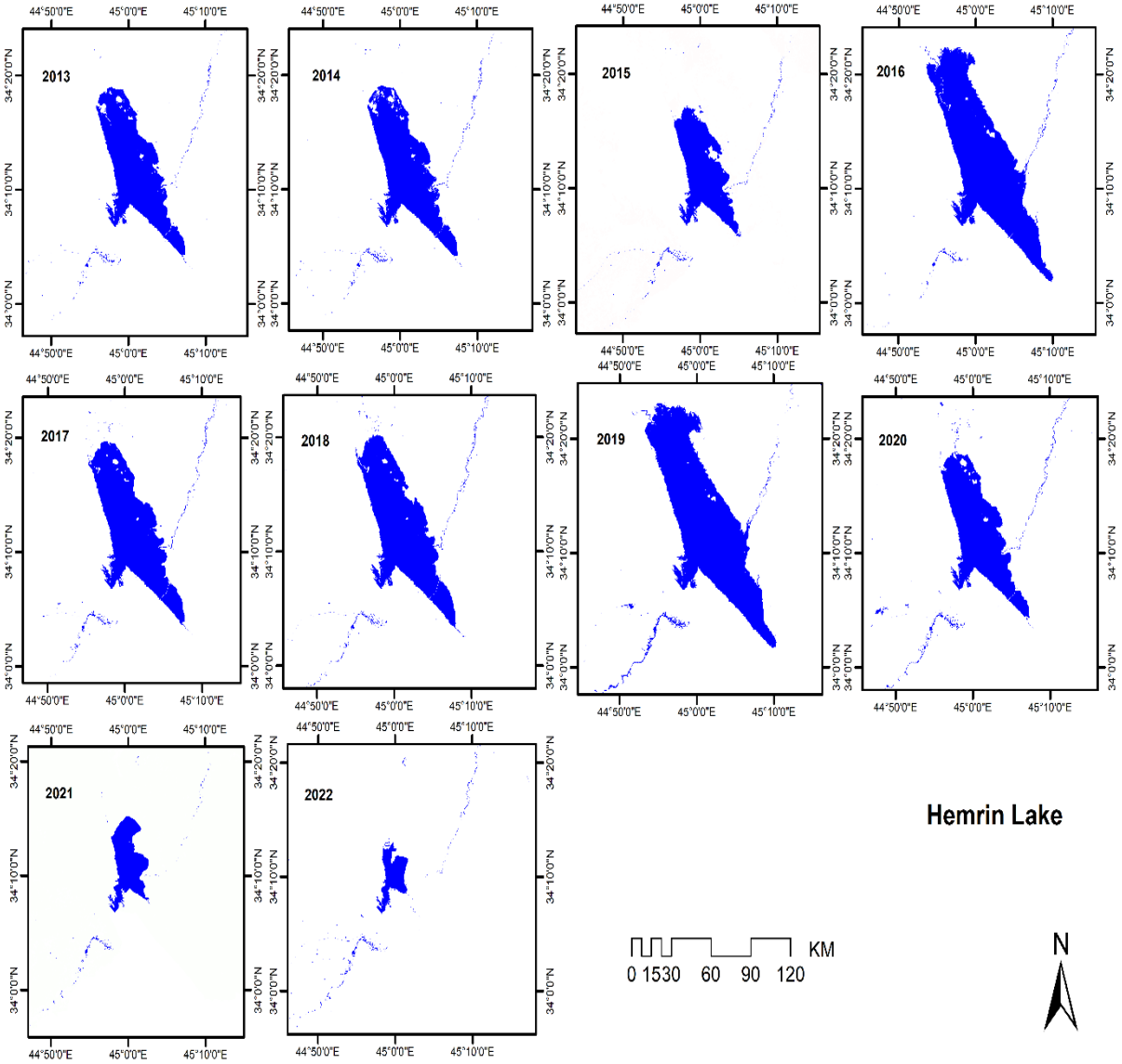

Figure 4.11 Changes in the surface area of Hemrin Lake (HLK) between 2013 and 2022.

4.7 Changes of NDBI and their Relationship to LST

Using ArcGIS software, the build-up index was located using the NDBI values. The NDBI values in the study area increased significantly in 2022. This is a result of increasing urban land and increasing barren areas . The computed NDBI values for the urban regions' spatial layout in the years 2013, 2016, 2019, and 2022 are shown in Figure 4.12.

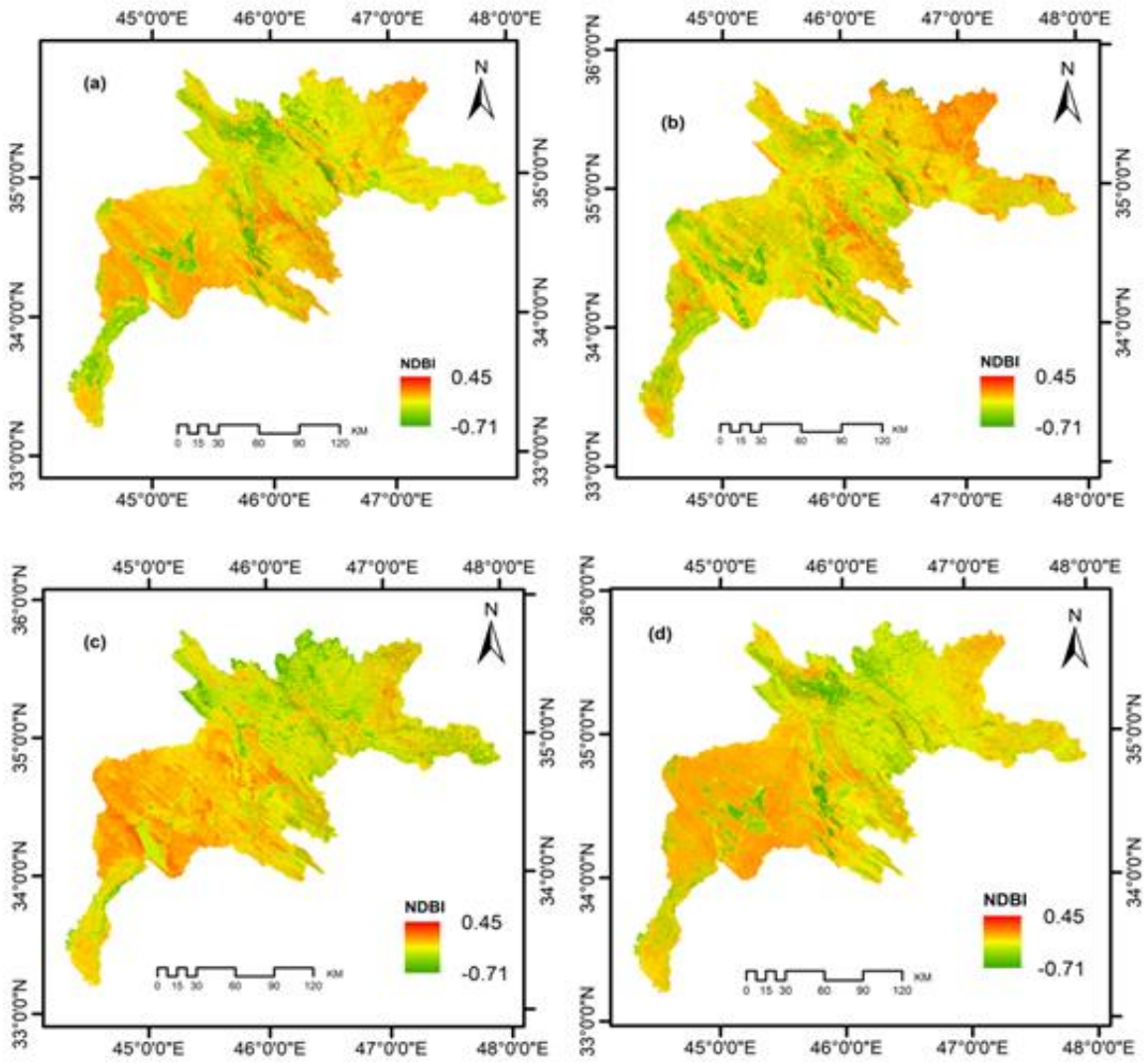

Figure 4.12 The Normalized Difference Built-up changes values of the Diyala Basin throughout (a) 2013; (b) 2016; (c) 2019; and (d) 2022.

Lower NDBI values depict vegetated regions like forests, crop fields, agricultural lands, parks, and water bodies, whereas higher NDBI values show urban areas like buildings, roads, bare soil, residential, and commercial areas. The study's findings suggest that places with greater LST were those where higher NDBI values were found. R^2 values of 0.66, 0.69, 0.68, and 0.74 were estimated to indicate a positive association between NDBI and LST for the years 2013, 2016, 2019, and 2022, respectively as shown in (Figure 4.13). LST and NDBI have a substantial positive correlation, which suggests that LULCs with more biomass have lower LST. findings also indicate that LST values are

lower in less NDBI regions, such as vegetation areas, but higher in more NDBI regions, such as built-up areas.

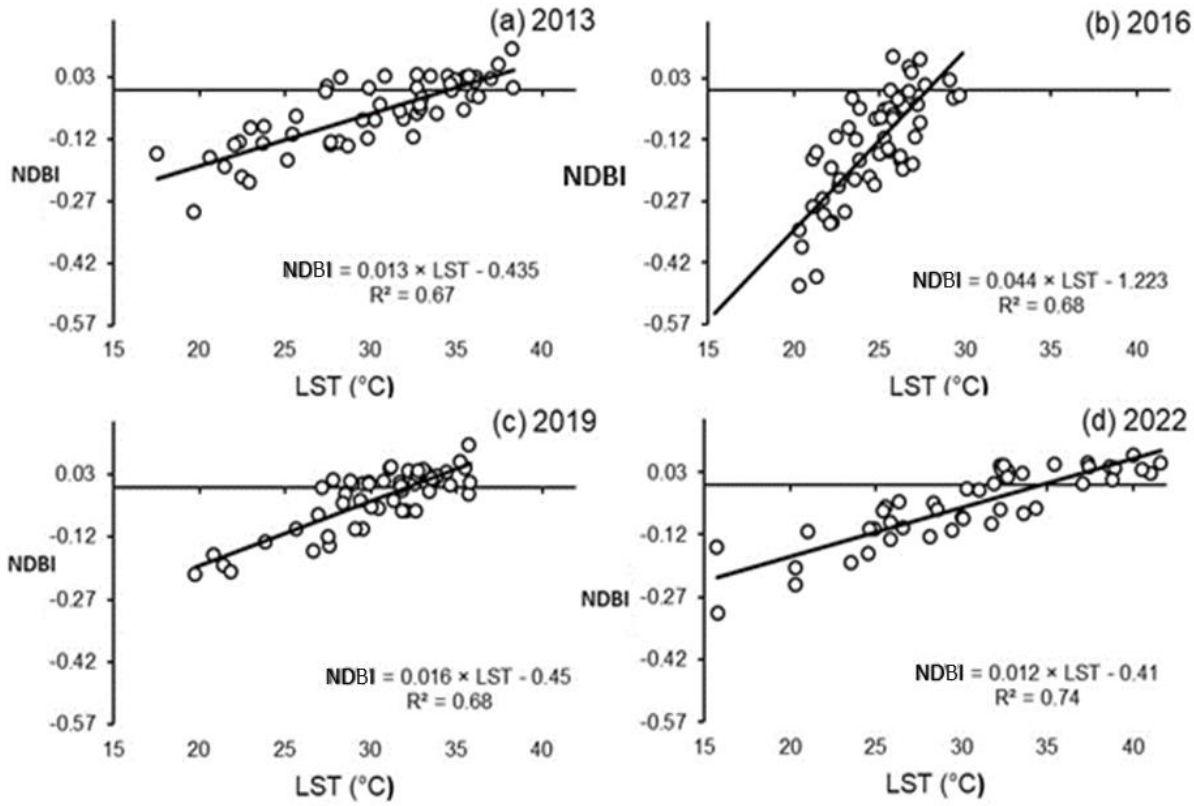

Figure 4.13 Alteration maps of the Normalized Difference Built-up Index (NDBI) and Land Surface Temperature (LST) of the Diyala Basin in (a) 2013; (b) 2016; (c) 2019; and (d)2022.

4.8.1 The SAVI changes and relation with LST

The Soil Adjusted Vegetation Index (SAVI) is important for vegetation detection based on the Natural Variation Vegetation Index (NDVI). The highest SAVI values indicate healthy and dense vegetation, while the lowest SAVI values indicate sparse plants and bare soil. The SAVI scale goes from -1 to 1. The level of pixel greenness, which indicates that there are sufficient organisms that can grow inside the pixel, is represented by the greatest SAVI value (which is very close to 1). A low SAVI score (around -1) denotes a pixel with little green content.

On average, between 2013 and 2022, the minimum values of SAVI decreased from -0.38 to -0.44, and the maximum values of SAVI increased from 0.91 to 0.97 (Figure 4.14). In 2013 and 2016, the maximum value of SAVI was 0.91,

showing that vegetation covers, such as grasslands and forest areas, had been expanded, while the minimum SAVI values were -0.38 and -0.42, in that order, revealing that DRB had a sufficient amount of water bodies. Between 2019 and 2022, the maximum values of SAVI were 1 and 0.97, indicating that the modified vegetation of the soil had expanded, and the minimum values of SAVI were -0.38 and -0.44, in that order, implying sufficient bodies of water and bare soil. Linear regression analysis was used to detect correlations between LST and SAVI, and the results showed that LST and SAVI were negatively correlated with regression analysis (Figure 4.15).

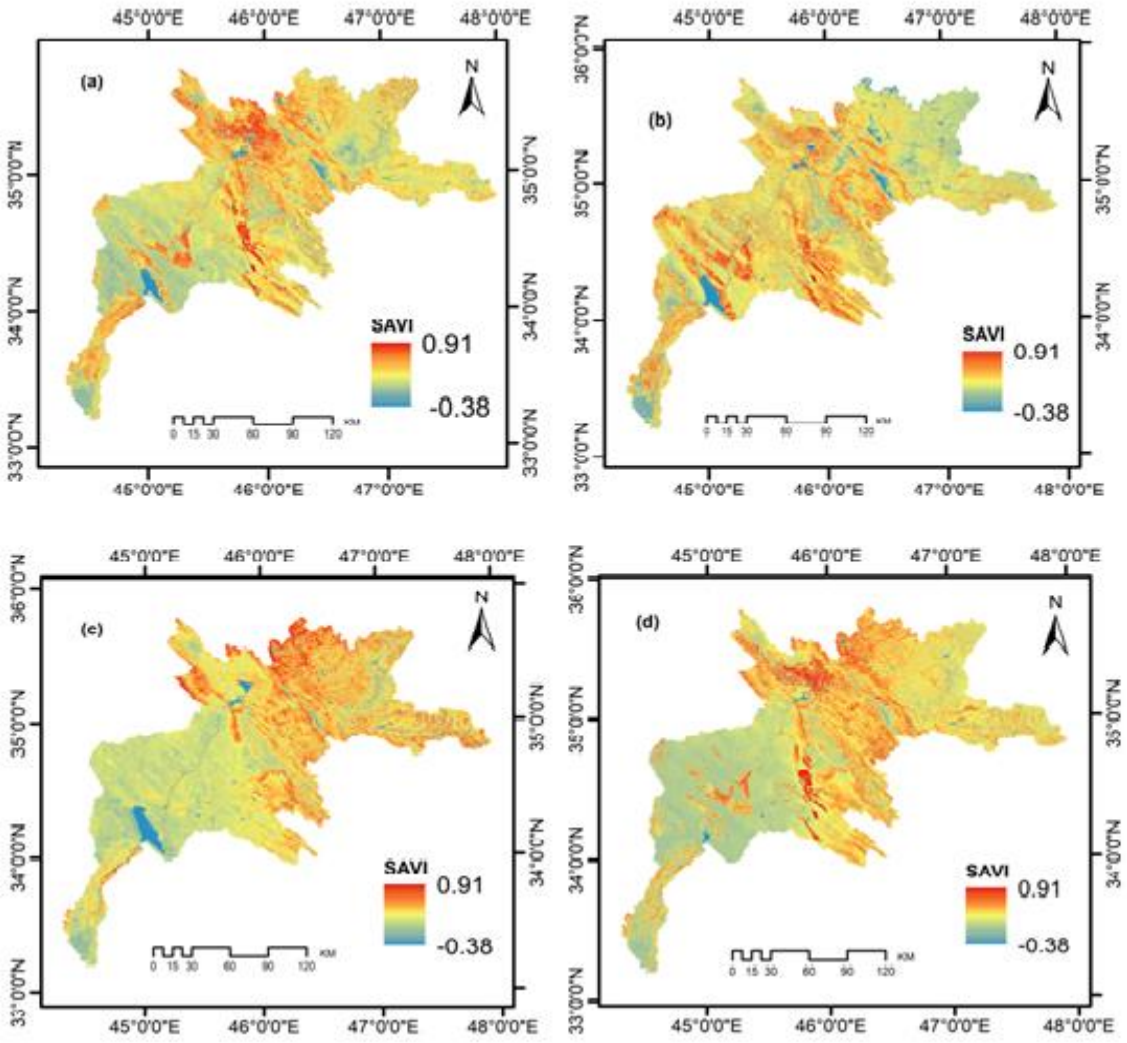

Figure 4.14 The Soil adjusted vegetation index changes values of the Diyala Basin throughout (a) 2013; (b) 2016; (c) 2019; and (d) 2022.

The direction of SAVI depends on the physical and chemical parameters of the leaves, the texture of the plant, and the value of L, where L is a correction factor with a value between 0 and 1. If the vegetation density is too great, the value 0 is utilized; if it is extremely low, the value 1 is used. Due to the study area's average plant density level, the adjustment factor utilized in this study has a value of 0.5. While LST is influenced by temperature, soil moisture, and soil particle size.

4.8.2 Comparison between NDVI and SAVI indices

The values for the indices were compared to land surface temperature to determine a correlation between the indices (Figure 4.15 and Figure 4.4). The results indicate that SAVI has a better correlation when compared to the NDVI index, where the value of R^2 is 0.82, 0,87, 0.77, and 0.83 during 2013, 2016, 2019, and 2022, in that order, for the SAVI index, whereas the NDVI index has a value of R^2 of 0.66, 0,64, 0.68, and 0.63 during 2013, 2016, 2019, and 2022, in that order. However, the SAVI index was adopted for the production of vegetation maps in order to reduce the effects of the soil background (Huete, 1988; Masoud and Koike, 2006).

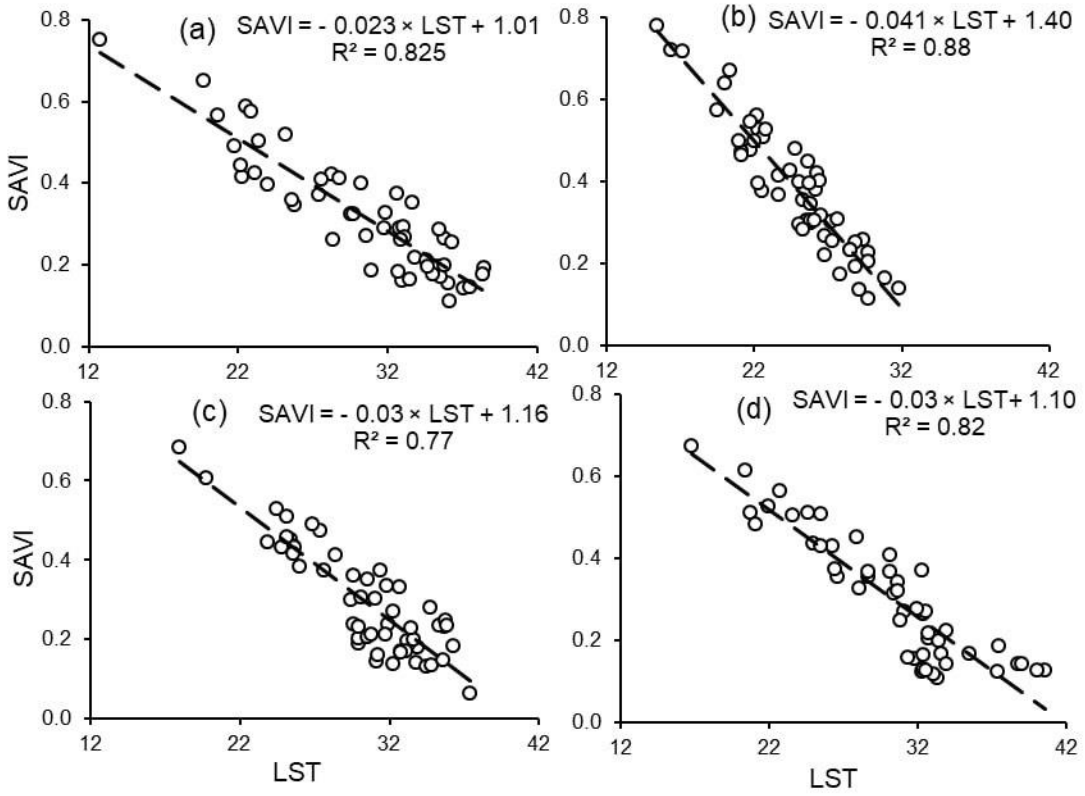

Figure 4.15 Alteration maps of the Soil adjusted vegetation index (SAVI) and Land Surface Temperature (LST) of the Diyala Basin throughout (a) 2013; (b) 2016; (c) 2019; and (d)2022.

CHAPTER FIVE
CONCLUSIONS AND RECOMMENDATIONS

5.1 Conclusions

In the present study, land use and land cover (LU and LC) patterns were delineated using remote sensing data and GIS technologies to assess and detect their changes in the Diyala River Basin (DRB) between 2013 and 2022, and therefor the following conclusion points can be drawn :-

1. The major cover the study area are vegetation cover , which covers 25273.9 km^2, 18914.5 km^2, 20983.8 km^2, and 22421.8 km^2, or roughly 76.6%, 57.4%, 63.6%, and 68.0% in 2013, 2016, 2019, and 2022, respectively.
2. From 2013 to 2022, agriculture decreased from 76.6% to 68.0%.
   Barren land and built-up land coverage were 3.93% and 17.5%, respectively, in 2013, but they increased to 5.1% and 25.8%, respectively, in 2022.
3. In low-density plant regions, there was a 4.5% drop in vegetation cover between 2013 and 2022. But with a ratio of around 5.9%, the area devoid of vegetation displayed an increased trend.
4. NDVI distributions are frequently impacted by meteorological factors, including temperature and precipitation.
5. According to NDVI, the amount of vegetation coverage fell by 20.67% and 36.33%, respectively, between 2021 and 2022.
   The levels of the Derbendekan and Hemrin lakes decreased by 15.1%, 7.12%, 108.38%, and 143.33% in 2021 and 2022, respectively.

The DRB had an increase in the frequency and severity of drought over the previous ten years, particularly in 2021 and 2022; a decrease in water body surface area; and a fall in precipitation averages. The findings of this study will aid in improving basin development and organisation and increasing water resources.

5.2 Recommendations

1. Investigate the changing LULC classes utilising more satellites, imageries sourced from Sentinel, MODIS and the quickbird with higher spatial resolution.
2. Integrated with the effects of climate change on LU and LC outlines in the future projection.
3. The absence of high-resolution images, which could alter the reliability of the findings, and the necessity for more thorough research with 1-year time intervals to comprehend the dynamics of the LU and LC changes are some of the study's drawbacks. To solve the aforementioned issues and provide greater information, more research is required.
4. Extending the study area and coverage period to include more regions and watersheds in Iraq.

References

Al-Faraj, F. A., & Scholz, M. (2014). Assessment of temporal hydrologic anomalies coupled with drought impact for a transboundary river flow regime: the Diyala watershed case study. Journal of Hydrology, 517, 64-73.

Al-Faraj, F. A., & Scholz, M. (2015). Impact of upstream anthropogenic river regulation on downstream water availability in transboundary river watersheds. International Journal of Water Resources Development, 31(1):28-49.

Almamalachy, Y.S., Al-Quraishi, A.M.F., Moradkhani, H., 2020. Agricultural drought monitoring over Iraq utilizing MODIS products. Environmental remote sensing and GIS in Iraq, 253-278.

Al-Najjar, H. A., Kalantar, B., Pradhan, B., Saeidi, V., Halin, A. A., Ueda, N., & Mansor, S. (2019). Land cover classification from fused DSM and UAV images using convolutional neural networks. Remote Sensing, 11(12):1461.

Al-Quraishi, A. M. F., Gaznayee, H. A. A., & Messina, J. P. (2021). Drought severity trend analysis based on the Landsat time-series dataset of 1998-2017 in the Iraqi Kurdistan Region. In IOP Conference Series: Earth and Environmental Science (Vol. 779, No. 1, p. 012083). IOP Publishing.

Al-Quraishi, A.M.F., Negm, A.M., 2019. Environmental remote sensing and GIS in Iraq. Springer-Water, Springer, Cham.

Al-Quraishi, A.M.F., Sadiq, H.A., Messina, J.P., 2019. Characterization and modeling surface soil physicochemical properties using Landsat images: A case study in the Iraqi Kurdistan region. The International Archives of the Photogrammetry, Remote Sensing and Spatial Information Sciences, 42, 21-28.

Al-Saady, Y., Merkel, B., Al-Tawash, B., Al-Suhail, Q. (2015). Land use and land cover (LULC) mapping and change detection in the Little Zab River Basin (LZRB), Kurdistan Region, NE Iraq and NW Iran. FOG-Freiberg Online Geoscience, 43.

AL-Timimi, Y. K., George, L. E., & AL-Jiboori, M. H. (2012). Drought risk assessment in Iraq using remote sensing and GIS techniques. Iraqi Journal of Science, 53(4):1078-1082.

References

Amalo, L. F., Hidayat, R., Sulma, S. (2018). Analysis of agricultural drought using vegetation health index Journal of Agricultural Science, 40:63-73

Anderson BJ, Hardy EE, Roach J T, Witmer RE (1976) A Land Use And Land Cover Classification System For Use With Remote Sensor Data. U.S. Geological Survey Professional Paper 964 (Vol. 2001).

Arsyad M, Tiwow VA, Rampe MJ (2018, November) Analysis of magnetic minerals of iron sand deposit in Sampulungan Beach, Takalar Regency, South Sulawesi using the x-ray diffraction method. In J Phys Conf Ser 1120(1): 012060. IOP Publishing.

Assaf AT, Sayl KN, Adham A (2021, August) Surface Water Detection Method for Water Resources Management. In J Phys Conf Ser 1973(1): 012149. IOP Publishing.

Breiman, L. (2001). Random forests. Machine learning, 45(1):5-32.

Camargo FF, Sano EE, Almeida CM, Mura JC, Almeida T (2019) A comparative assessment of machine-learning techniques for land use and land cover classification of the Brazilian tropical savanna using ALOS-2/PALSAR-2 polarimetric images. Remote Sens 11(13):1600

Campbell JB (2007) Introduction to remote sensing, 4th edn. The Guilford Press, New York

Camps-Valls G, Benediktsson JA, Bruzzone L, Chanussot J (2011) Introduction to the issue on advances in remote sensing image processing. IEEE J Sel Top Signal Process 5(3):365–369.

Chopra, P., 2006, January. Drought risk assessment using remote sensing and GIS: a case study of Gujarat. Enschede, The Netherlands: ITC.

Congalton RG (1991) A review of assessing the accuracy of classifications of remotely sensed data. Remote Sens Environ. https://doi.org/10.1016/0034-4257(91)90048-B

Congalton, R. G., & Green, K. (2019). Assessing the accuracy of remotely sensed data: principles and practices. CRC press.

Congedo, L. (2021). Semi-Automatic Classification Plugin: A Python tool for the download and processing of remote sensing images in QGIS. Journal of Open Source Software, 6(64):3172.

References

Daba, M. H., & You, S. (2022). Quantitatively assessing the future land-use/land-cover changes and their driving factors in the upper stream of the Awash River based on the CA–markov model and their implications for water resources management. Sustainability, 14(3):1538.

Degife, A., Worku, H., Gizaw, S., Legesse, A., 2019. Land use land cover dynamics, its drivers and environmental implications in Lake Hawassa Watershed of Ethiopia. Remote Sens. Appl.: Soc. Environ., 14, 178–190 .https://doi.org/10.1016/j.rsase.2019.03.005

Dewidar KM (2004) Detection of land use/land cover changes for the northern part of the Nile delta (Burullus region), Egypt. Int J Remote Sens 25(20):4079–4089

Dibaba, W. T., Demissie, T. A., Miegel, K. (2020). Drivers and implications of land use/land cover dynamics in Finchaa catchment, northwestern Ethiopia. Land, 9(4):113. https://doi.org/10.3390/land9040113.

Eklund, L., Pilesjo, P., 2012. Migration Patterns in Duhok Governorate, Iraq, 2000-2010. Open Geogr. J., 5.(1)

ESRI, (2020). ArcGIS Desktop: Release (10.8). Environmental Systems Research Institute, Redlands.

FAO (1998a) Food and Agriculture Organization of the UN. Adaptation to climate change in semi-arid environments. Retrieved from http://www.fao.org/docrep/015/i2581e/i2581.

Foley, J.A., Levis, S., Costa, M.H., Cramer, W., Pollard, D., 2000. Incorporating dynamic vegetation cover within global climate models. Ecol. Appl. 10(6), 1620-1632

Foody GM. (2002) Status of land cover classification accuracy assessment. Remote Sensing of Environment, 80(1), 185–201.

Gaznayee, H. A. A, Al-Quraishi, A. M. F, Mahdi K, & Ritsema, C. (2022). A Geospatial Approach for Analysis of Drought Impacts on Vegetation Cover and Land Surface Temperature in the Kurdistan Region of Iraq. Water, 14(6):927.

Gaznayee, H. A., & Al-Quraishi, A. M. F. (2019). Analysis of agricultural drought's severity and impacts in Erbil Province, the Iraqi Kurdistan region based on time series NDVI and TCI indices for 1998 through 2017. Jour of Adv Research in Dynamical & Control Systems, 11(11):287-297.

References

Gaznayee, H.A.A., Al-Quraishi, A.M.F., Al-Sulttani, A.H.A., 2021. Drought Spatiotemporal

Gorelick, N., Hancher, M., Dixon, M., Ilyushchenko, S., Thau, D., & Moore, R. (2017). Google Earth Engine: Planetary-scale geospatial analysis for everyone. Remote sensing of Environment, 202:18-27.

Goward, S. N., Xue, Y., & Czajkowski, K. P. (2002). Evaluating land surface moisture conditions from the remotely sensed temperature/vegetation index measurements: An exploration with the simplified simple biosphere model. Remote Sensing of Environment, 79(2-3):225-242.

Goward, S.N., Xue, Y., Czajkowski, K.P., 2002. Evaluating land surface moisture conditions from the remotely sensed temperature/vegetation index measurements: An exploration with the simplified simple biosphere model. Remote Sens. Environ., 79(2-3), 225-242.

Green L, Fry AF, Myerson J (1994) Discounting of delayed rewards: a life-span comparison. Psychol Sci 5(1):33–36. https://doi.org/10.1111/j.1467-9280.1994.tb00610.x

Hagos, M. K., Egilson , D., Bjornsson, B. B., Thorarinsdottir, T., Gudmundsson, J. (2014). Analysing the effect of Land Use Land Cover change on catchment discharge, Land Restoration Training Programme Keldnaholt, 112 Reykjavik, Iceland.

Hailu, Y., Tilahun, B., Kerebeh, H., Tafese, T., 2018. Land use land cover change detection in Gibe Sheleko National Park, Southwestern Ethiopia. J. Agric. Resour. Econ. 4(1868–2019–381), 20–30 .https://doi.org/10.22004/ag.econ.281757

Haque MI, Basak R (2017) Land cover change detection using GIS and remote sensing techniques: a spatio-temporal study on Tanguar Haor, Sunamganj, Bangladesh. Egypt J Remote Sens Space Sci 20(2):251–263. https://doi.org/10.1016/j.ejrs.2016.12.003

Huete, A. R. (1988). A soil-adjusted vegetation index (SAVI). Remote Sensing of Environment, 25(3):295-309.

Hussain, M., Tayyab, M., Zhang, J., Shah, A. A., Ullah, K., Mehmood, U., & Al-shaibah, B. (2021). Gis-based multi- criteria approach for flood vulnerability assessment and mapping in district Shangla: Khyber Pakhtunkhwa, Paki- stan. Sustainability (Switzerland), 13(6). https://doi.org/10.3390/SU13063126

References

Hussain, S., & Karuppannan, S. (2023). Land use/land cover changes and their impact on land surface temperature using remote sensing technique in district Khanewal, Punjab Pakistan. Geology, Ecology, and Landscapes, 7(1):46-58.

Hussain, S., Mubeen, M., Ahmad, A., Fahad, S., Nasim, W., Hammad, H. M., ... & Parveen, S. (2021). Using space–time scan statistic for studying the effects of COVID-19 in Punjab, Pakistan: A guideline for policy measures in regional agriculture. Environmental Science and Pollution Research, 1-14.

Hussain, S., Mubeen, M., Karuppannan, S., 2022. Land use and land cover (LULC) change analysis using TM, ETM+ and OLI Landsat images in district of Okara, Punjab, Pakistan. Phys. Chem. Earth A/B/C, 103117 .https://doi.org/10.1016/j.pce.2022.103117

Hussain, S., Mubeen, M., Sultana, S. R., Ahmad, A., Fahad, S., Nasim, W., ... & Ali, M., (2022). Managing greenhouse gas emission. In Modern Techniques of Rice Crop Production (pp. 547-564). Singapore: Springer Singapore.

Huyen, N. T. (2016). Assessing the impacts of land use and climate change on soil and water resources in the Srepok watershed, Central Highland, Vietnam. Policy Brief Series - Southeast Asian Regional Center for Graduate Study and Research in Agriculture (SEARCA), 2.

Islam, K., Jashimuddin, M., Nath, B., & Nath, T. K. (2018). Land use classification and change detection by using multi-temporal remotely sensed imagery: The case of Chunati wildlife sanctuary, Bangladesh. The Egyptian Journal of Remote Sensing and Space Science, 21(1):37-47.

Jamali A (2019) Evaluation and comparison of eight machine learning models in land use/land cover mapping using Landsat 8 OLI: a case study of the northern region of Iran. SN Appl Sci 1(11):1–11

Jensen, J. R. (2005). Introductory Digital Image Processing: A Remote Sensing Perspective. 3rd Edition, Prentice Hall, Upper Saddle River, 505-512.

Julien, Y., & Sobrino, J. A. (2010). Comparison of cloud-reconstruction methods for time series of composite NDVI data. Remote Sensing of Environment, 114(3):618-625.

References

Juliev, M., Pulatov, A., Fuchs, S., Hübl, J., (2019). Analysis of Land Use Land Cover Change Detection of Bostanlik District,Uzbekistan. Polish Journal of Environmental Studies, 28(5). https://doi.org/10.15244/pjoes/94216.

Khwarahm, N. R., Najmaddin, P. M., Ararat K, & Qader, S. (2021a). Past and future prediction of land cover land use change based on earth observation data by the CA–Markov model: a case study from Duhok governorate, Iraq. Arabian Journal of Geosciences 14(15):1-14.

Khwarahm, N. R., Qader, S., Ararat, K., & Al-Quraishi, A. M. F. (2021b). Predicting and mapping land cover/land use changes in Erbil/Iraq using CA-Markov synergy model. Earth Science Informatics, 14(1):393–406. https://doi.org/10.1007/s12145-020-00541-x.

Koc D, Ikiel C, Atalay A, Ustaoglu B (2012) Land use and land cover (LULC) classification using spot-5 image in the Adapazari plain and its surroundings, Turkey. Online J Sci Technol 2:37–42

Lee, S.H., Yoo, S.H., Choi, J.Y., Bae, S., 2017. Assessment of the impact of climate change on drought characteristics in the Hwanghae Plain, North Korea using time series SPI and SPEI: 1981–2100. Water 9(8), 579.

Lin, X., Xu, M., Cao, C., Singh, P.R., Chen, W., Ju, H., 2018. Land-use/land-cover changes and their influence on the ecosystem in Chengdu City, China during the period of 1992–2018. Sustainability, 10(10), 3580. https://doi.org/10.3390/su10103580

Lu, D., Mausel, P., Brondizio, E., & Moran, E. (2004). Change detection techniques. International Journal of Remote Sensing, 25(12):2365-2401.

Mohammed, R., Scholz, M., 2017a. Adaptation strategy to mitigate the im- pact of climate change on water resources in arid and semi-arid regions: a case study. Water Resource. Manag. 31, 3557–3573.

Mohammed, R., Scholz, M., 2017b. Impact of evapotranspiration formulations at various elevations on the reconnaissance drought index. Water Resource. Manag. 31, 531–548.

Mohammed, R., Scholz, M., 2019. Climate variability impact on the spatiotemporal characteristics of drought and Aridity in arid and semi-arid regions. Water Resource. Manag. 33 (15), 5015–5033.

References

Mahdi, Z. A., & Mohammed, R. (2022). Land use/land cover changing aspect implications: Lesser Zab River Basin, northeastern Iraq. Environmental Monitoring and Assessment, 194(652):1-16. https://doi.org/10.1007/s10661-022-10324-0.

Masoud, A. A., & Koike, K. (2006). Arid land salinization detected by remotely-sensed landcover changes: A case study in the Siwa region, NW Egypt. Journal of arid environments, 66(1), 151-167.

Maxwell AE, Warner TA, Fang F (2018) Implementation of machine-learning classification in remote sensing: an applied review. Int J Remote Sens 39(9):2784–2817

McFeeters, S. K. (1996). The use of the Normalized Difference Water Index (NDWI) in the delineation of open water features. International Journal of Remote Sensing, 17(7):1425-1432.

Menon, D. K., Bhavana, V., 2016. An overview of Drought evaluation and monitoring using remote sensing and GIS. Pdfs. Semantic scholar. Org, 3(5), 32-37.

Mohammed OA, Sayl KN (2021) A GIS-based multicriteria decision for groundwater potential zone in the west desert of Iraq. IOPConf Ser: Earth Environ Sci 856(1):012049

Mohammed SS, Sayl KN, Kamel AH (2022) Ground water recharge mapping in Iraqi Western Desert. Int J Des Nat Ecodyn 17(6):913-920. https://doi.org/10.18280/ijdne.170612

Mohammed SS, Sayl KN, Kamel AH (2022) Ground water recharge mapping in Iraqi Western Desert. Int J Des Nat Ecodyn 17(6):913–920. https:// doi. org/ 10. 18280/ ijdne. 170612

Mohammed, J., 2013. Land use and cover change assessment using Remote Sensing and GIS: Dohuk City, Kurdistan, Iraq (1998–2011). Int. j. geomat. geosci., 3(3), 552

Mohy HAA, Rasheed KG (2022) Morphological perspective of urban resilience through eco urban landscape: Iraq -Basra as a case study. Int J Des Nat Ecodyn 17(6):807–821. https:// doi. org/ 10. 18280/ ijdne. 170601

Mustafa, Y., 2020. Spatiotemporal analysis of vegetation cover in Kurdistan region-Iraq using MODIS image data. J. appl. sci. technol. trends, 1(1), 01-07.

Mustafa, Y.T., Ismail, D.R., 2019. Land use land cover change in Zakho District, Kurdistan Region, Iraq: past, current and future. In 2019 International Conference on Advanced Science and Engineering (ICOASE) (pp. 141-146). IEEE

References

Mustafa, Y.T. 2015. Mapping and Estimating Vegetation Coverage in Iraqi Kurdistan Region using Remote Sensing and GIS; Iraq-Final Report; Prepared and Implemented by Applied Remote Sensing & Gis (Ars&Gis) Center, University Of Zakho, Salahaddin University, University of Garmian, and Directorate of Forests and Range in Duhok; General Directorate of Horticulture, Forestry and Rangeland, Ministry of Agriculture and Water Resources: Erbil, Kurdistan Region, Iraq,; pp. 1–136.

Naqi NM, Al-Madhhachi AST, Al-Jiboori MH (2022) Quantifying Diyala River basin rainfall-runoff models for normal and extreme weather events. Water Pract Technol 17(8):1553-1569

Naqi, N. M., Al-Jiboori, M. H., Al-Madhhachi, A. S. T. (2021). Statistical analysis of extreme weather events in the Diyala River basin, Iraq. Journal of Water and Climate Change, 12(8):3770-3785.

Peijun, S., Aihui, W., Fubao, S., Ning, L., Tao, Y., Wei, X., ... & Hongjian, Z. (2016). A study of global change population and economic system risk forming mechanism and assessment. Advances in Earth Science, 31(8):775.

Pradhan, B., Al-Najjar, H. A., Sameen, M. I., Tsang, I., & Alamri, A. M. (2020). Unseen land cover classification from high-resolution orthophotos using integration of zero-shot learning and convolutional neural networks. Remote Sensing, 12(10):676.

Rajendran, G. B., Kumarasamy, U. M., Zarro, C., Divakarachari, P. B., & Ullo, S. L. (2020). Land-use and land-cover classification using a human group-based particle swarm optimization algorithm with an LSTM Classifier on hybrid pre-processing remote-sensing images. Remote Sensing, 12(24), 4135.

Richards, J.A. (1993) Remote Sensing Digital Image Analysis: An Introduction. Springer-Verlag, Berlin, 340 p. https://doi.org/10.1007/978-3-642-88087-2

Saleh, A.M., Ahmed, F.W., 2021. Analyzing Land Use/Land Cover Change Using Remote Sensing and GIS in Mosul District, Iraq. Ann. Romanian Soc. Cell Biol., 4342–4359. https://www.annalsofrscb.ro/index.php/journal/article/view/1928

Sameer YM, Abed AN, Sayl KN (2021) Highway route selection using GIS and analytical hierarchy process case study Ramadi Heet rural highway. J Phys Conf Ser 1973(1):012060

References

Sameer YM, Abed AN, Sayl KN (2023) Geomatics-based approach for highway route selection. Appl Geo mat 15(1):161–176

Sayl KN, Sulaiman SO, Kamel AH, Al-Ansari N (2022) Towards the Generation of a Spatial Hydrological Soil Group Map Based on the Radial Basis Network Model and Spectral Relectance Band Recognition. Int J Des Nat Ecodyn 17(5):761–766

Schnepf, R. D., 2004, June. Iraq agriculture and food supply: background and issues. Congressional Research Service, Library of Congress.

Singh A (1989) Review article digital change detection techniques using remotely sensed data. Int J Remote Sens 10(6):989–1003

Sun, Q., Tan, J., & X.u. Y. (2010). An ERDAS image processing method for retrieving LST and describing urban heat evolution: a case study in the Pearl River Delta Region in South China. Environmental Earth Sciences, 59(5):1047-1055.

Talib R, Shamkhi MS (2022). Impact of Climate Change on Integrated Management of Water Resources in The lower Basin of Diyala River, Iraq. Wasit J Eng Sci 10(3):145-160

Talukdar S, Singha P, Mahato S, Praveen B, Rahman A (2020) Dynamics of ecosystem services (ESs) in response to land use land cover (LU/LC) changes in the lower Gangetic plain of India. Ecol Ind 112:106121

Tembo,N., & Volk, J. (2022). Effects of Land-Use Land-Cover Change on River flow in Chalimbana River Catchment,Chongwe District, Zambia. International Journal of Innovative Science and Research Technology, ISSN No: 2456-2165.

Thomlinson JR, Bolstad PV, Cohen WB (1999) Coordinating Methodologies for Scaling Landcover Classifications from Site-Specific to Global. Remote Sensing of Environment, 70(1), 16–28. doi:10.1016/S0034-4257(99)00055-3

Viera, A. J., & Garrett, J. M. (2005). Understanding inter observer agreement: the kappa statistic. Family Medicine, 37(5), 360-363. PMID: 15883903.

Weng Q (2002) Land-use change analysis in the Zhujiang Delta of China using satellite remote sensing, GIS, and stochastic modeling. J Environ Manage 64(3):273–284.

References

Winnaar, G., Jewitt, G. P. W., & Horan, M. (2007). A GIS-based approach for identifying potential runoff harvesting sites in the Thukela River basin, South Africa. Physics and Chemistry of the Earth, Parts A/B/C, 32(15-18):1058-1067.

Wright GG, Morrice JG (1997) Landsat TM spectral information to enhance the land cover of Scotland 1988 dataset. International Journal of Remote Sensing, 18(18), 3811–3834. doi:10.1080/014311697216630.

Yesuph, A.Y., Dagnew, A.B., 2019. Land use/cover spatiotemporal dynamics, driving forces and implications at the Beshillo catchment of the Blue Nile Basin, North Eastern Highlands of Ethiopia. Environ. Syst. Res., 8(21), 1–30. https://doi.org/10.1186/s40068-019-0148-y.

Zha, Y., Gao, J., & Ni, S. (2003). Use of normalized difference built-up index in automatically mapping urban areas from TM imagery. International journal of remote sensing, 24(3), 583-594.

Zakaria, S., Mustafa, Y., Mohammed, D., Ali, S., Al-Ansari, N., Knutsson, S., 2013. Estimation of annual harvested runoff at Sulaymaniyah Governorate, Kurdistan region of Iraq. J. Nat. Sci. 5(12), 1272-1283.

Zhang, L., Jiao, W., Zhang, H., Huang, C., & Tong, Q. (2017). Studying drought phenomena in the Continental United States in 2011 and 2012 using various drought indices. Remote Sensing of Environment, 190:96-106.

الخلاصة

الجفاف من الكوارث التي تؤثر تأثيرا عميقا على عدة عوامل، بما في ذلك الاقتصاد والزراعة والبيئة والمجتمع. ولرصد حالات الجفاف بنجاح في المناطق شبه القاحلة، يلزم إجراء تقييمات لشدة الجفاف وتأثيره. ومع ذلك، لا يُعرف سوى القليل عن كيفية تأثير الاختلافات في الأنماط والتكوينات السنوية لاستخدام الأراضي والغطاء الأرضي (LULC) على عواقب الجفاف. تم تقييم تصنيف LULC وتطور الجفاف ورسم خرائط له من خلال الجمع بين نظام المعلومات الجغرافية وتقنيات الاستشعار عن بعد. يعتبر حوض نهر ديالى (DRB)، شمال العراق، منطقة دراسة تمثيلية. تم رسم خرائط لخمسة أنواع رئيسية من LULC: المسطحات المائية، والأراضي الحضرية، والأراضي العارية، والأراضي النباتية، والنخيل، اعتمادًا على صور Landsat للأعوام 2013 و2016 و2019 و2022. وتم تصنيف الصور باستخدام خوارزمية التصنيف وطريقة الاحتمالية القصوى. أظهرت نتائج الدراسة أنه خلال فترة الدراسة توسعت الأراضي الحضرية والأراضي العارية من 1295.8 كم2 (3.9%) إلى 1677.4 كم2 (5.1%) ومن 5770.3 كم2 (17.5%) إلى 8501.1 كم2 (25.8%)، في حين بلغ الغطاء النباتي وانخفضت مساحة الأراضي من 25,273.9 كيلومتر مربع (76.6%) إلى 22,421.8 كيلومتر مربع (68.0%). باستخدام المؤشرات الطيفية من لاندسات، قام البحث الحالي أيضًا بتقييم حجم وتكرار حالات الجفاف في DRB خلال موسم النمو لعام 2013 حتى عام 2022. تم إنشاء خمسة عشر فسيفساء على مدى عشر سنوات باستخدام أربعين صورة في لاندسات (8 و 9 OLI/TIRS) (36/167 و37/168)) التي تم جمعها من عام 2013 إلى عام 2022. المشاهد مأخوذة من سلسلتين زمنيتين من نوع Landsat. تم تقييم حالة الجفاف باستخدام مؤشر الفرق الطبيعي للغطاء النباتي (NDVI)، ومؤشر حالة الغطاء النباتي (VCI)، ومؤشر الغطاء النباتي المعدل للتربة ، ومؤشر الفرق الطبيعي للمياه, ودرجة حرارة سطح الأرض (LST). كشفت نتائج البحث عن ارتفاع في حدوث الجفاف في منطقة DRB وشدة الجفاف خلال السنوات العشر الماضية، خاصة في عامي 2021 و2022. ومع ذلك، بين عامي 2021 و2022، انخفض إجمالي الغطاء النباتي بناءً على مؤشر الغطاء النباتي للغطاء النباتي بنسبة 20.67% و36.33% على التوالي. وفي عامي 2021 و2022، انخفضت الأراضي النباتية بشكل ملحوظ (54.3% و29.5% على التوالي). وأظهرت نتائج VCI أنه في عام 2022، كان هناك جفاف شديد طويل الأمد بلغ 5727.1 كيلومتر مربع (47.8٪). إن مؤشر NDVI ومؤشر LST مرتبطان بشكل وثيق بمؤشرات الجفاف وهما مناسبان للاستخدام في المناطق القاحلة وشبه القاحلة لرصد الجفاف ببيانات محدودة. وشهدت بحيرتا دربندخان وحمرين، على حد سواء، انخفاضات بنسبة 15.1% و7.12% و108.38% و143.33% في عامي 2021 و2022 على التوالي. بين عامي 2013 و2022، شهدت منطقة DRB زيادة في الجفاف، وانخفاضًا في مساحة سطح الجسم

المائي، وانخفاضًا في متوسطات هطول الأمطار. وستعمل هذه الدراسة على تعزيز معرفة الروابط بين مؤشرات الجفاف المستمدة من الاستشعار عن بعد والأرصاد الجوية.

جمهورية العراق
وزارة التعليم العالي والبحث العلمي
جامعة بابل/ كلية الهندسة
قسم الهندسة المدنية

تأثيرات تغير الطقس الإقليمي على استخدام الأراضي ـ الغطاء الأرضي باستخدام نظم المعلومات الجغرافية

رسالة مقدمة إلى قسم الهندسة المدنية، كلية الهندسة، جامعةِ بابل
وهي جزء مِنْ متطلبات الحصول على درجة الماجستير علوم في
الهندسة/ الهندسة المدنية / الموارد المائية

من قبل:

محمد حسين يونس حسين

بأشراف:

أ.د. رقية كاظم محمد

الميلادي 2023 **الهجري 1445**